

ANALYSIS OF ELECTRICAL SIGNATURES  
IN SYNCHRONOUS GENERATORS  
CHARACTERIZED BY BEARING FAULTS

A Thesis

by

JAE-WON CHOI

Submitted to the Office of Graduate Studies of  
Texas A&M University  
in partial fulfillment of the requirements for the degree of  
MASTER OF SCIENCE

December 2006

Major Subject: Mechanical Engineering

ANALYSIS OF ELECTRICAL SIGNATURES  
IN SYNCHRONOUS GENERATORS  
CHARACTERIZED BY BEARING FAULTS

A Thesis

by

JAE-WON CHOI

Submitted to the Office of Graduate Studies of  
Texas A&M University  
in partial fulfillment of the requirements for the degree of

MASTER OF SCIENCE

Approved by:

Chair of Committee, Alexander G. Parlos  
Committee Members, Edgar Sanchez-Sinencio  
Bryan Rasmussen

Head of Department, Dennis O'Neal

December 2006

Major Subject: Mechanical Engineering

## ABSTRACT

Analysis of Electrical Signatures in Synchronous Generators Characterized by  
Bearing Faults. (December 2006)

Jae-Won Choi, B.E., Korea University, Seoul, South Korea

Chair of Advisory Committee: Dr. Alexander G. Parlos

Synchronous generators play a vital role in power systems. One of the major mechanical faults in synchronous generators is related to bearings. The popular vibration analysis method has been utilized to detect bearing faults for years. However, bearing health monitoring based on vibration analysis is expensive. One of the reasons is because vibration analysis requires costly vibration sensors and the extra costs associated with its proper installation and maintenance. This limitation prevents continuous bearing condition monitoring, which gives better performance for rolling element bearing fault detection, compared to the periodic monitoring method that is a typical practice for bearing maintenance in industry. Therefore, a cost effective alternative is necessary. In this study, a sensorless bearing fault detection method for synchronous generators is proposed based on the analysis of electrical signatures, and its bearing fault detection capability is demonstrated.

Experiments with staged bearing faults are conducted to validate the effectiveness of the proposed fault detection method. First, a generator test bed with an *in-situ* bearing damage device is designed and built. Next, multiple bearing damage experiments are carried out in two vastly different operating conditions in order to obtain statistically significant results. During each experiment, artificially induced bearing current causes accelerated damage to the front bearing of the generator. This *in-situ* bearing damage process entirely eliminates the necessity of disassembly

and reassembly of the experimental setup that causes armature spectral distortions.

The electrical fault indicator is computed based on stator voltage signatures without the knowledge of machine and bearing specific parameters. Experimental results are compared using the electrical indicator and a vibration indicator that is calculated based on measured vibration data. The results indicate that the electrical indicator can be used to analyze health degradation of rolling element bearings in synchronous generators in most instances. Though the vibration indicator enables early bearing fault detection, it is found that the electrical fault indicator is also capable of detecting bearing faults well before catastrophic bearing failure.

To My Mother

## ACKNOWLEDGMENTS

I would like to convey my sincere thanks and gratitude to my committee chair and advisor, Dr. Alexander G. Parlos, for his patience, continuous guidance, technical support and advice through the course of my research work. I also thank Dr. Edgar Sanchez-Sinencio and Dr. Bryan Rasmussen for their time, interest and support in my research.

Finally, I would like to acknowledge and thank, all the students at NIML, especially, Parasuram, Lin, Aninda, and Dan for several insightful discussions on related and unrelated topics, alike.

## TABLE OF CONTENTS

CHAPTER		Page
I	INTRODUCTION . . . . .	1
	A. Motivation . . . . .	1
	B. An Introduction to the Electrical Signature Analysis and the Motor Current Signature Analysis . . . . .	3
	1. Background History and Applications . . . . .	3
	2. Principles . . . . .	4
	C. Literature Review . . . . .	4
	1. Sensorless Fault Detection of Mechanical Defects in Generators . . . . .	5
	a. Time and Frequency Analysis Approaches . . . . .	5
	b. Model Based Approach . . . . .	6
	2. Sensorless Fault Detection of Generalized Rough- ness Bearing Faults in Induction Motors . . . . .	6
	3. Classification of Bearing Faults . . . . .	7
	a. Single Point Defects . . . . .	7
	b. Generalized Roughness . . . . .	7
	c. Single Point Defect and Practicality Issue . . . . .	8
	4. Off-line Bearing Fault Seeding and <i>In-situ</i> Bearing Damage Process . . . . .	8
	D. Research Objectives . . . . .	9
	E. Proposed Approach . . . . .	10
	F. Thesis Contributions . . . . .	11
	G. Organization of the Thesis . . . . .	12
II	DESCRIPTION OF THE EXPERIMENTAL SETUP . . . . .	13
	A. Introduction . . . . .	13
	B. Synchronous Generator and Its Auxiliary Equipment . . . . .	13
	1. Synchronous Generator . . . . .	13
	a. Operating Principles of a Synchronous Generator	17
	b. Disabled Functions: Voltage Regulation and Three Phase Rectification . . . . .	18
	c. Stator . . . . .	19

CHAPTER	Page
d. Rotor . . . . .	20
e. Carbon Brushes . . . . .	21
f. Sheave and Fan . . . . .	21
g. Bearings . . . . .	22
h. Front and Rear Body Units . . . . .	23
2. The Induction Motor and AC Motor Drive . . . . .	24
3. The V Belt . . . . .	26
4. Miscellaneous Mechanical Parts . . . . .	27
5. The Field Excitation Power Supply . . . . .	28
6. The Electrical Load . . . . .	28
C. Sensors and Data Acquisition Systems . . . . .	29
1. Armature Voltage Sensors . . . . .	29
2. Armature Current Sensors . . . . .	31
3. Field Voltage and Current Sensors . . . . .	31
4. Vibration Sensor . . . . .	31
5. Data Acquisition Hardware . . . . .	32
6. Data Acquisition Software . . . . .	32
D. <i>In-situ</i> Bearing Damage Device . . . . .	33
1. Mechanism of Rolling Element Bearing Failure due to Shaft Current . . . . .	35
2. Variable AC Transformer . . . . .	36
3. Power Resistors and Shunt Resistors . . . . .	36
4. Carbon Brush . . . . .	37
E. Chapter Summary . . . . .	39
III DESCRIPTION OF THE EXPERIMENTAL PROCEDURES . . . . .	40
A. Introduction . . . . .	40
B. Preparation for the Experiments . . . . .	40
1. Bearing Reconditioning and Installation . . . . .	40
2. Generator Assembly, Mounting, Belt Tension Ad- justment and Alignment . . . . .	42
3. Field Current . . . . .	43
4. Bearing Damage Current Magnitude . . . . .	44
5. Parameter Settings in the Data Acquisition Program . . . . .	45
C. Execution of the Experiments . . . . .	46
1. Setting of the Different Operating Conditions . . . . .	46
2. Experimental Plan Table . . . . .	47
3. Experimental Timetable . . . . .	48



CHAPTER	Page
	49
IV	50
	50
	50
	52
	52
	52
	55
	58
	59
	59
	59
	61
	61
	61
	68
	69
	72
V	73
	73
	74
	74
REFERENCES	76
VITA	82

## LIST OF TABLES

TABLE		Page
I	NI DAQ channel allocation. . . . .	33
II	Summary of experimental plan and parameter settings. . . . .	48
III	Comparison of healthy baselines. . . . .	60
IV	Comparison of bearing failure times. . . . .	69
V	Comparison of estimated bearing fault detection times. . . . .	70

## LIST OF FIGURES

FIGURE	Page
1	The synchronous generator and its auxiliary equipment after installation on a moving cart. . . . . 14
2	Picture of the synchronous generator, its auxiliary equipment, and the carbon brush mount after installation on a moving cart. . . . . 15
3	Picture of the electrical load and sensor circuits. . . . . 15
4	Cut-away view of the synchronous generator. . . . . 16
5	Four types of ball bearing misalignment [9]. . . . . 25
6	Circuit diagram of the whole electrical systems. . . . . 30
7	Flowchart of data acquisition algorithm. . . . . 34
8	Picture of the bearing damage device, (a) current injection circuit (b) bearing damage carbon brush. . . . . 35
9	<i>In-situ</i> bearing damage circuit installation and shaft current path. . . 38
10	Carbon brush installation issues. . . . . 39
11	Data processing flow chart. . . . . 51
12	Flow chart of the main data processing routine. . . . . 53
13	Voltage signatures before and after leakage minimization at 40 Hz operation. . . . . 56
14	Indicator comparison plot for a 20 Hz case study; experiment #3. . . 62
15	Indicator comparison plot for a 40 Hz case study; experiment #4. . . 63
16	Electrical indicator plot for a 40 Hz case study; experiment #1. . . . 65
17	Indicator comparison plot for a 20 Hz case study; experiment #4. . . 66

FIGURE	Page
18      Electrical indicator plot for a 20 Hz case study; experiment #2. . . .	67
19      Electrical indicator plot for a 40 Hz case study; experiment #5. . . .	67

## CHAPTER I

### INTRODUCTION

#### A. Motivation

Synchronous generators play a vital role in power systems [1], [2]. From fossil-fueled power plants to renewable source power plants such as wind farms, synchronous generators has been extensively used to convert mechanical energy to electrical energy for decades. Auxiliary power generators are often installed in buildings to provide electricity in case of power outages [3], [4]. More recently, hybrid technology in the automotive industry has become increasingly popular due to high cost of gasoline where a key mechanical component is the motor-generator [5], [6].

Failure of such generators potentially causes bigger financial losses besides the repair costs since our society largely depends on reliable sources of electricity. For example, factories will suffer unscheduled downtime and lost production during a power outage. Auxiliary power failures during a power outage such as in public infrastructure, such as telecommunication systems, computer networks, and emergency facilities like fire service installations will threaten the reliable daily operation of our society to a large extent [4]. Therefore, early detection of an imminent failure of such generators is of great importance in order to improve the reliability of power systems [1].

About 60% of all faults in electrical machines are related to malfunctions of mechanical components, such as bearings, shafts and so on [1]. A recent reliability survey on small diesel and gas-turbine power systems shows that bearing related faults account for about 30% of total generator faults in stability auxiliary diesel-

---

The journal model is *IEEE Transactions on Automatic Control*.

generators [3]. However, it is noted that only limited literature is found on the subject of generator reliability survey due to time-consuming and expensive data collection. Grasselli also states that lack of interest in disclosing generator reliability survey data from companies or institutions is part of the reason since the data potentially indicates the quality of critical management of them [4], [7]. In contrast, several reliability surveys on bearing faults in induction motors are found in literature. One of the statistics by General Electric and IEEE Industry Applications Society shows that over 40% of over 100 hp motor failures are associated with bearing faults [8], [9].

A variety of bearing fault detection & diagnosis techniques have been proposed for generators and motors. They include wear particle analysis [10], ultrasonic analysis [11], breakaway and coast-down analysis [12], thermography analysis [13], magnetic flux analysis [14], and vibration analysis [15]. Vibration analysis is further divided into probabilistic analysis, time-domain analysis, and the most popular frequency domain analysis. The frequency domain analysis is again divided into bearing defect frequency method, high frequency shock pulse and friction method, and enveloped spectrum method, and so on [16].

The largest industrial machines, equipped with sleeve bearings and built-in diagnosis sensors, receive the benefits of the above-mentioned fault diagnosis techniques. However, some of those techniques are not suitable for smaller electrical machines, which are often equipped with rolling-element bearings and have no built-in vibration sensors due to higher production and maintenance costs [9], [17]. Nonetheless, vibration signature analysis has become the most common fault detection & diagnosis techniques for the rolling element bearing faults in small electrical machines [16], [18].

Vibration signature analysis, however, has several disadvantages. Firstly, it requires at least one vibration sensor and the extra costs for its proper installation & maintenance. Secondly, a technician needs knowledge and a good amount of expe-

rience to correctly use such sensors. Thirdly, it utilizes detailed machine-dependent information, such as bearing dimensions and machine rotational speeds, which field operators often do not have access to. Lastly, the interpretation of the results often requires expert involvement. Moreover, bearing health monitoring using vibration sensors for electric machines is costly. In industry, bearing health of such electric machines is monitored periodically rather continuously due to economical reasons even though continuous bearing health monitoring gives better performance in bearing fault detection. Hence, in order to avoid some of these problems, alternatives such as the Motor Current Signature Analysis (MCSA) and the Electric Signature Analysis (ESA) have been proposed.

## B. An Introduction to the Electrical Signature Analysis and the Motor Current Signature Analysis

### 1. Background History and Applications

The MCSA and the ESA were originally developed at the Oak Ridge National Laboratory for fault diagnosis of electric motors and the driven devices [19], [20]. The MCSA technique was initially applied to motor-operated valves in nuclear power plant safety systems for assessment of aging and wear. Later it was successfully applied to fault diagnosis of various types of motor driven equipment such as pumps, blowers, and air-conditioning systems [21]. The ESA technique was also utilized in health assessments of AC and DC motors, and more recently, other electro-mechanical machines like alternators and generators. This technique also performs the analysis of mechanical performance of motor driven systems, such as valves, pumps, compressors, and mechanical and hydraulic couplings [19].

## 2. Principles

Both the MCSA and the ESA techniques are based on the usage of an electric machine as a permanently installed transducer. Such a transducer senses mechanical load and speed variations in the driven systems or electric machine itself and convert them via back-emf into stator signal variations. The stator signals are collected in a non-intrusive manner and then processed to detect and diagnose mechanical and electrical faults in electric machines and the driven systems.

In the MCSA technique, only electrical stator current measurements are collected and processed to identify small variations in the current signatures [21]. Though this technique provides direct information of presence of abnormal conditions in electric machines, the quantification of fault severity has been an open problem, thereby resulting in utilizing voltages for additional information [22].

The ESA technique, however, utilizes not only stator current signals but also stator voltage signals. In this technique, stator current and voltage signals are processed to identify defect frequencies in the signatures or to calculate power factors, real, reactive, apparent powers, voltage rms, and current rms in one phase or more phases. It has been shown that ESA indicators after proper processing are sensitive to mechanical and electrical disturbances occurring in motors and its driven devices [12], [19].

### C. Literature Review

Limited literature has been found on the subject of fault diagnosis of mechanical defects in generators using the ESA [15]. The literature is ever more scarce for rolling element bearing faults in synchronous generators. For electrical motors, however, the situation is different. Bearing fault diagnosis in induction motors, for example, has



flourished in the last decade as evidenced by numerous published articles [14], [23], [24], [25], [26], [27]. Considering the many similarities in electric machines, some of the proposed MCSA and ESA techniques for electrical motors can serve as a guideline for this research on synchronous generators.

## 1. Sensorless Fault Detection of Mechanical Defects in Generators

### a. Time and Frequency Analysis Approaches

The phase voltage waveform of an automotive alternator with rotor rubbing defect is shown slightly different from the baseline waveform in the comparison plots [19], [28]. It is shown that the harmonic distortion level in the output voltage signature of a rotor tachometer generator of a Bell Jet Ranger helicopter has a correlation with the level of rotor blade unbalance. Some of the voltage signature components in the starter-generator of the helicopter are shown to be sensitive to mechanical loads as well as rotor blade unbalance. In airline integrated drive generator experiments, it is observed that the amplitudes of frequency signature components associated with a gear mesh increase when a load level is increased, or a bad gear mesh is installed.

These simple comparison results in the time and frequency domains show the feasibility of the ESA to detect mechanical faults. However, these techniques depend on either identifying non-stationary frequency components in a voltage signature or comparing time signals directly. Hence, the method's limitations include the requirement of knowing detailed machine data, lack of automated calculation method, and difficulty involved in interpretation of the results.

## b. Model Based Approach

A model based fault diagnosis technique is proposed for dynamic eccentricity fault detection in salient pole synchronous generators [1]. In the article, a theoretical electromagnetic coupling model is created based on modified winding function theory. Then the model is simulated with hypothetical machine parameters. The results show that the amplitudes of the 17th and 19th harmonics in the line current signature increase along with the severity of the dynamic eccentricity. The main limitations of this method include lack of experimental validation, the requirement of machine parameters, and the assumption of linear model and linear time invariant parameters, which can cause poor performance in practice.

## 2. Sensorless Fault Detection of Generalized Roughness Bearing Faults in Induction Motors

One untold common limitation of the above-mentioned approaches is that they are only intended for identifying single point defects. A model based bearing fault diagnosis of induction motors is proposed in [25] and this method is intended for detecting both single point defects and generalized roughness faults. In the beginning, a notch filtering process is added in order to improve the robustness of the indicator. In the process, major frequency components unrelated to bearing condition are removed from the stator current signature using full knowledge of machine parameters. It is noted that the remaining signature preserves bearing condition information including any faults. Then a baseline spectrum is estimated via autoregressive estimation and a spectral deviation of faulty spectrum from the baseline spectrum is calculated. As the bearing becomes degraded, the spectral deviation is shown to be increased.

However, the main drawback of this method is that the notch filtering process

requires knowledge of machine parameters just like frequency analysis methods. Moreover, the proposed fault indicator shows poor fault detection performance at middle and high loadings due to large variations.

### 3. Classification of Bearing Faults

As mentioned above, faults in rolling element bearings can be classified into two groups: single point defects and generalized roughness [29]. Brief descriptions of each fault and associated issues are discussed here based on [29].

#### a. Single Point Defects

A single point defect in a rolling element bearing is a single and localized bearing defect caused by a pit or a spall on race tracks, balls, or/and a train. It produces a distinctive vibration frequency according the location of a defect. The vibration is transmitted through the bearing housing, sometimes the characteristic vibration frequencies appear on stator signatures after being modulated by the electrical fundamental frequency.

#### b. Generalized Roughness

Generalized roughness, however, is not a localized defect. Rather it is caused by surface roughness, deformed rolling elements, wrapped raceways, and etc, which are typically not visible to naked eyes. The bearings with this fault spins roughly or with difficulty typically accompanying with increased machine vibration. Unlike single point defects, generalized roughness does not generate a specific characteristic vibration frequency. Hence, bearing frequency identification technique can not be used.

### c. Single Point Defect and Practicality Issue

Vibration frequency analysis in the literature traditionally focuses on detecting single point defects as discussed in the previous sections. This trend continues as MCSA and ESA techniques are being developed. Most of the proposed MCSA and ESA bearing fault detection techniques are intended for diagnosis of single point defects only, even though single point defects are rare in practice [26]. Because of this reason, there is a large discrepancy between highly advanced bearing detection techniques for single point defects in the literature and their lack of use in industry [29]. It is noteworthy that some newly published papers admit this issue even though they focus on this rare type of bearing fault in their papers [27], [30].

## 4. Off-line Bearing Fault Seeding and *In-situ* Bearing Damage Process

Most of the staged bearing fault detection experiments in the literature utilize off-line fault seeding to damage bearings. In such experiments, a hole is drilled on the outer raceway to emulate outer race defects. The balls with notches on the surfaces emulate ball defects [27]. This process often causes unwanted types of bearing damages such as deformed raceways and a wrapped train. Moreover, it inevitably requires disassembling, reassembling, remounting, and realigning of a test machine. Reassembly and reinstallation process dramatically alters stator and rotor vibration signatures so that it is difficult to obtain a consistent healthy signature to compare. The detailed descriptions of these adverse effects are found in [31]. Most of the literature disregards this adverse aspect of off-line fault seeding, and thereby, the experiment results suffer from inconsistencies.

In order to avoid these disadvantages, two *in-situ* bearing damage processes have been proposed: electric discharge machining method (EDM) [31] and foreign material

injection method (FMI) [30]. In EDM, a large amount of external current is injected through a rotor shaft. A grease film between the balls and raceways behaves as a capacitor and a sudden burst of discharged current in the capacitor causes a real damage on the raceway. In FMI, fine foreign materials are directly injected while a test machine is running.

There are more limitations to FMI than EDM. The FMI method is hard to apply to smaller electric machines whose tight geometries cause difficulty in access for damaging bearings. Moreover, it has not been proven that FMI causes a similar type of damage to raceways and balls compared to a naturally damaged bearings. Even though the EDM method is dangerous, EDM enables to control the damage speed through current magnitude and the access problem of the FMI is not an issue for the EDM. Moreover EDM is one of the common bearing damage processes in industry [32], [33], [34], so this damage process represents a natural bearing damage process.

#### D. Research Objectives

From the previous sections, it is seen that there is a strong need for a practical sensorless fault detection method for rolling element bearings in synchronous generators. Some of the requirements include minimal use of machine parameters, simple calculations in the fault indicator, and easy interpretation of the results.

The objectives of this research are listed as follows:

- to design & build a generator test bed with an *in-situ* bearing damage device based on [31], and the associated data acquisition system;
- to set up an experimental plan and conduct experiments accordingly;

- to analyze bearing faults using signatures obtained from electrical measurements;
- to compare electrical fault signatures with comparable vibration signatures;

This research does not address the many issues related to the development and testing of a fault diagnosis system, such as the false alarming rates and optimization of detector performance.

#### E. Proposed Approach

A synchronous generator is obtained by disabling the voltage regulator and three phase voltage rectifier of an automotive alternator. The field is energized by an external power supply. The stator winding is modified so that the output signal measurements are collected via a data acquisition system. Three armature terminals are connected to a three resistor bank that functions as an external electrical loading.

The generator is driven by a three phase induction motor through a soft coupling, which reduces harmonic distortion. A heavy metal plate serves as a base for the generator and the induction motor, and it also functions as a vibration absorber for them.

An *in-situ* bearing damage process is used to avoid the disadvantages of the off-line fault injection method. A bearing damage device is constructed using a variable AC transformer, ballast resistors and shunt resistors based on [31].

An experiment plan is set up with two groups of experiments. The operating conditions of one group differs from the operating conditions of the other. Each group consists of five experiments for repeatability of results.

Stator line currents and phase voltages, rotor field current and voltage, and three axis vibration measurements are collected via a data acquisition system. The

experimental data are saved in files.

Experimental data are reloaded from a file at a time. Stator measurements are conditioned in the time domain and they are converted into the frequency domain using the FFT. The average power is then be calculated to check whether the signal is stationary. Large odd harmonics and some inter-harmonics are removed from the signature without using machine parameters. Due to spectral distortions in the stator signals caused by mechanical disturbances from the faulty bearing, the remaining signature contains information on comprehensive bearing conditions; therefore, both single point defect and generalized roughness faults can be detected. After removing proper harmonics, the average power of the remaining signature is calculated and it constitutes the fault indicator. Machine vibration data are conditioned in the time domain and an average rms of vibration signals are calculated. It serves as a comparison references to the electrical fault indicator.

## F. Thesis Contributions

The main contributions of this work are summarized as follows:

- A synchronous generator test-bed with an *in-situ* bearing damage circuit is designed and built.
- Bearing health deterioration in a synchronous generator is analyzed based on electrical signatures characterized by bearing faults utilizing a simple signal processing technique without the knowledge of any machine specific information, including machine and bearing parameters.

## G. Organization of the Thesis

In Chapter II, the experimental setups are explained in detail. In addition, the operating principles of synchronous generators and EDM are briefly discussed. In Chapter III, the detailed experimental procedures are discussed. They include the experimental preparatory procedures and the parameter settings in the experimental equipment. In Chapter IV, the data processing routines are explained in detail. Then, the experimental results are analyzed. In Chapter V, a summary of this thesis, conclusions of this research, and the future work are presented.



## CHAPTER II

### DESCRIPTION OF THE EXPERIMENTAL SETUP

#### A. Introduction

This chapter discusses the design principles, the physical dimensions, and the operating principles of the experimental setup used in this research. The experimental setup is divided into largely three groups: the synchronous generator and its auxiliary equipment, the sensors and the data acquisition system (DAQ), and the *in-situ* bearing damage device. Each apparatus is described in a separate section.

#### B. Synchronous Generator and Its Auxiliary Equipment

The auxiliary equipment is divided into the generator driving system including a soft coupling, the generator electrical accessories like the three resistor bank and the field power supply, and the miscellaneous mechanical components like a belt tension adjuster and an induction motor driving the alternator through the belt. The synchronous generator and its auxiliary equipment are depicted in Figs. 1 after installation on a moving cart. Fig. 2 shows the picture of the synchronous generator, its auxiliary equipment, and the carbon brush mount from the *in-situ* bearing damage device after installation on a moving cart. Fig. 3 shows the electrical load and the sensors for stator voltage and current measurements.

##### 1. Synchronous Generator

The synchronous generator of this research is obtained by modifying a Delco Remy CS-130 Lundell automotive alternator. The easy availability of this alternator and its internal replacement components in the automotive market, the small size, and

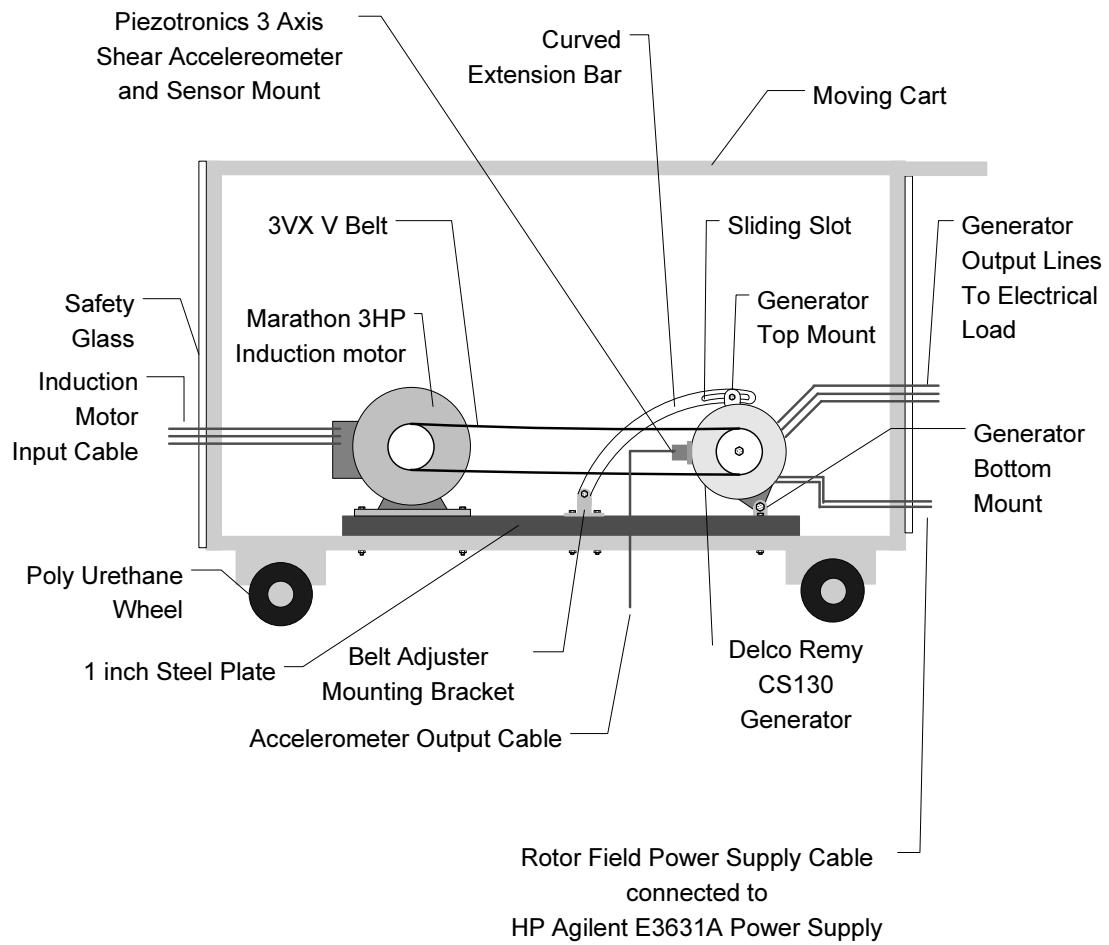


Fig. 1. The synchronous generator and its auxiliary equipment after installation on a moving cart.

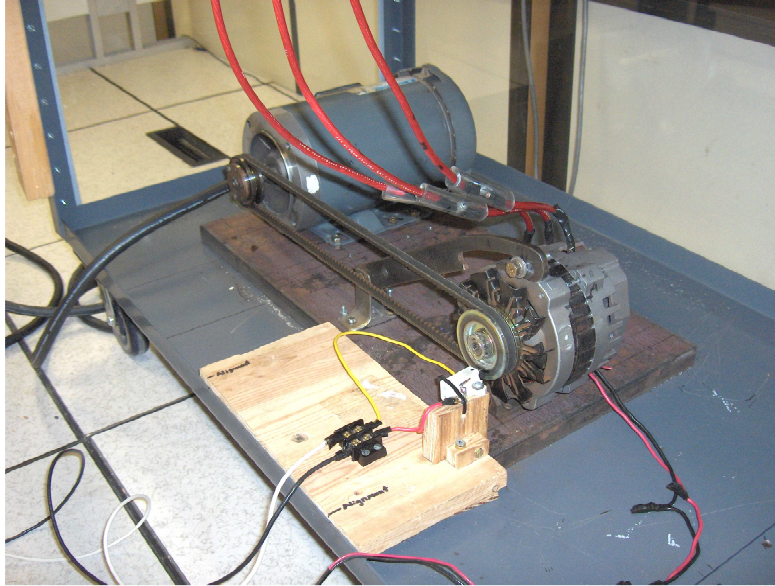


Fig. 2. Picture of the synchronous generator, its auxiliary equipment, and the carbon brush mount after installation on a moving cart.

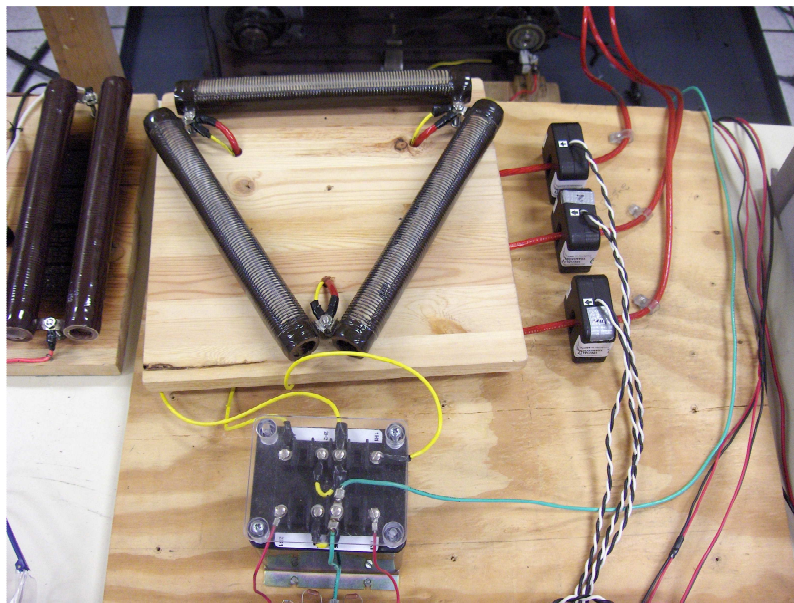


Fig. 3. Picture of the electrical load and sensor circuits.

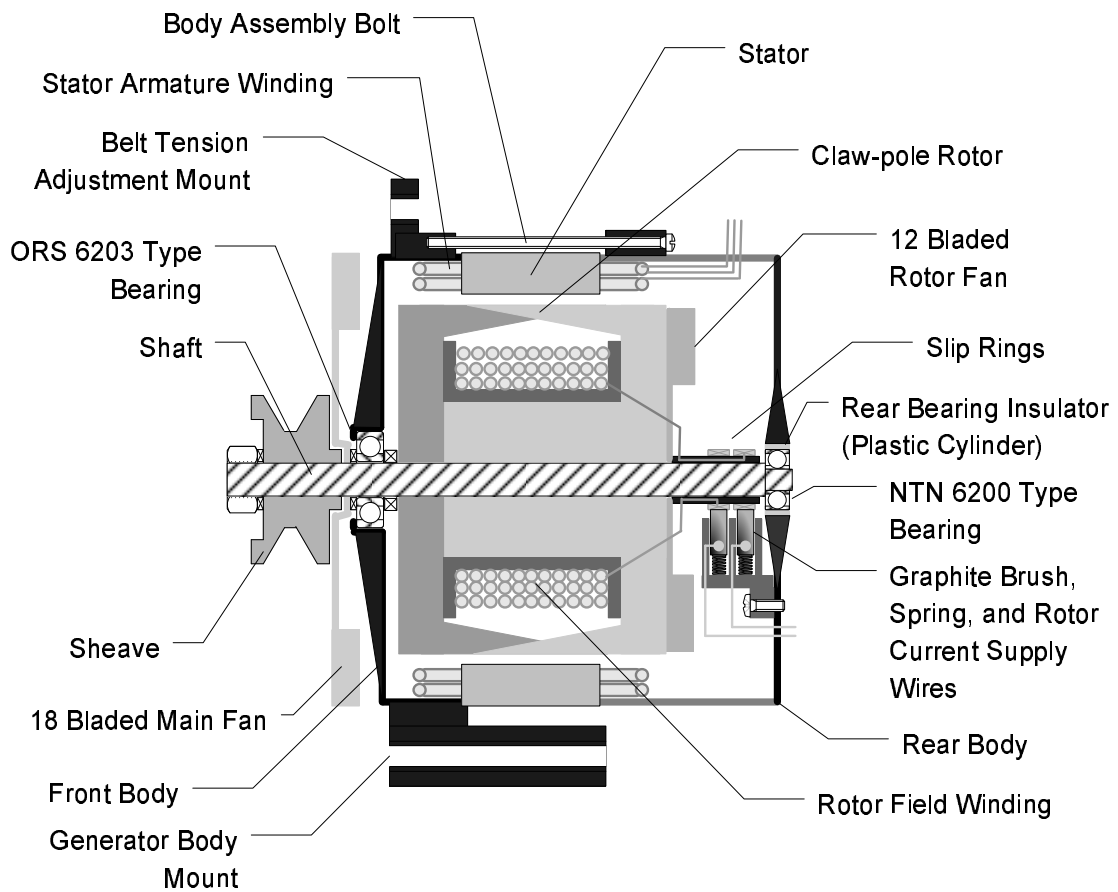


Fig. 4. Cut-away view of the synchronous generator.

the suitable output power rating are some of the main reasons for this choice. This synchronous generator consists of several internal components. The cut-away view of the generator is depicted in Fig. 4.

First the operating principles of synchronous generators are explained in a subsection. Then the dimensions, the design, and the operating principles of major internal components are discussed.

#### a. Operating Principles of a Synchronous Generator

Most of the content in this section is borrowed from [35]. The operating principles of synchronous generators can be described using a simple synchronous generator model.

The rotor field coil is energized by a direct current source and it produces a field magnetomotive force (MMF) around the rotor poles. Due to the MMF, the field magnetic flux crosses the air gap and enters the armature winding. When the rotor rotates at synchronous speed, the flux linkage with the stator winding induces the electromotive force (EMF) in the armature coils. If a electrical load is connected to the armature coil, the armature current flows and generates the armature reaction. The armature reaction MMF generates the armature flux. This armature flux and the field flux are superimposed to create a resultant flux, then resulting in a resultant EMF. The field MMF and the armature MMF rotate at a synchronous speed but the field MMF leads the armature MMF by the load angle, which is determined by the ratio of the reactance impedance to the resistance impedance of the armature winding and the electrical load. The misalignment of the two MMF's creates an electromagnetic torque that balances the driving torque from the input power source.

This simple model is different from a real synchronous generator in several aspects. In a real synchronous generator, the resulting flux density typically contains appreciable harmonics and the flux is shaped to be flat-topped rather than a pure

sinusoidal. One of the reasons for the harmonic distortion is that the difference in the armature reluctance in the armature slot and the armature tooth creates the ripples of flux density in the armature winding. Leakage flux is another difference. Some of the field flux does not cross the air gap and it accounts for the field leakage flux. This leakage is typically neglected in the analysis when an effective value of the field flux is used. Some of the armature flux results in slot leakage flux, end-turn leakage flux, and air gap leakage flux. These leakage terms are typically lumped together and considered as a fictitious leakage reactance.

#### b. Disabled Functions: Voltage Regulation and Three Phase Rectification

Most of the content in this subsection is borrowed from [36]. The main difference between automotive alternators and synchronous generators is that automotive alternators produce a DC voltage by using a 3- $\phi$  solid state rectifier and a built-in voltage regulator.

Most automotive alternators utilize a 3- $\phi$  armature winding for higher efficiency and less torque variations [35]. However, 3- $\phi$  AC power cannot be store in an automotive DC battery, nor it can be used to energize the 1- $\phi$  rotor field coil. Therefore, the 3- $\phi$  rectifier is used to convert the AC armature voltages into DC output.

An automotive alternator is typically driven by the engine through a V or serpentine belt, and two pulleys. Since the engine rotational speed varies over different driving conditions, the alternator output voltage also varies according to the speed. However, the battery terminal voltage must remain between 12V through 14V, thereby, regulation of the alternator output voltage is necessary. The detailed voltage regulation mechanism is as follows. A small built-in analog/digital circuit called automatic voltage regulator senses the output DC voltage of the 3- $\phi$  rectifier and compares the output voltage with a pre-defined desired value in the voltage reg-

ulator's microprocessor memory. Then it controls the duty cycle of the field current fed to the rotor coil. Therefore, the voltage regulator finally controls the MMF of the rotor magnetic field. The controlled MMF changes the flux linkage with the armature winding, the resultant EMF, and finally the terminal voltage.

The 3- $\phi$  rectification and automatic voltage regulation, however, are not suitable for this research due to the following reasons:

- Synchronous generators typically produce 3- $\phi$  AC output voltages.
- Control of the field current using Pulse Width Modulation (PWM) is not used in synchronous generators.
- The PWM of the field current using a Darlington circuit and the DC conversion using 6 solid state diodes in the 3- $\phi$  rectifier introduce unwanted harmonic distortion in the output voltage.
- A typical synchronous generator has more sophisticated terminal voltage control system utilizing the American Standards Association (ASA) method [35].
- The built-in automatic voltage regulation prevents precise control of the rotor MMF and the terminal voltages.

### c. Stator

The stator of this generator can be separated from the front and the rear units. It is shaped like a 5/8" thick open-ended hollow cylinder with 4-5/8" outer diameter and 1" length. It has two fitting grooves on the circumferences at both ends and they serve as assembly guides.

The three long coils form a delta winding in the stator. The inner side of the stator cylinder has the evenly spaced 36 longitudinal slots that accommodate a bundle

of 0.05” diameter enamel insulated copper wires. Each of the wires is wound around the stator slots in a zigzagging manner so that the winding looks like a square wave train along the stator cylinder circumference. The circumferential width of the wave train is about 1” and it matches with the circumferential width of a rotor pole in the rotor. The height of the wave is about 2” and it is same as the length of a rotor pole in the rotor. Inside of the wave, two rotor slots occupied by the other phase windings are placed. Since there is no neutral connection point in a delta winding, three terminals exist. Two ends of different phase coils are twisted to form a terminal connection, The three terminal connections are later linked to a 3- $\phi$  electrical load via the 8 AWG wires. It is noted that the stator windings are never rewound during this research, and the turn number of the stator windings are not counted.

#### d. Rotor

The rotor consists of two 3-3/4” diameter claw poles, a 5/8” diameter shaft, a pair of slip rings, and a rotor field winding between the two claw-poles. Each claw pole has six fingers of slightly different sizes. The claw pole finger looks like an equilateral triangle where the width and the height are about 1” and 1-1/2”, respectively. The two claw poles are assembled in a way that the opposite fingers have even 3/8” gaps between them. Between the two claw poles, the rotor field winding is located. The field coil is a long enamel coated copper wire wound in a small plastic cylinder. The two coil ends are linked to the copper slip rings on the rear shaft end. The slip rings are implanted in the plastic cylinder that are tightly fitted on the shaft. A 12 blade ventilation fan is located in the rear claw pole. This fan cools down the rotor while the energized field coil generates heat. The shaft diameter at the rear end is reduced to 3/8” and a smaller 6200 type bearing fits tightly into the spot. By trial and error, it is found that removing the rear bearing damages the slip rings.



The generator is equipped with a salient rotor called claw-pole rotor. This type of rotor is typical for automotive Lundell alternators. This type of rotor causes saliency effects on the armature signatures where third harmonics exist in signatures [35]. This rotor has 12 rotor poles while most synchronous generators have 2 or 4 rotor poles. Due to the six pair of fingers, a single mechanical rotation of the rotor produces six cycles of electric signals. Since the rotor MMF also depends on the geometry of the finger in the rotor, the asymmetric claw pole finger may produce unwanted harmonic distortion.

e. Carbon Brushes

Two carbon brushes connect the electrical wires from the excitation current supply to the rotor field coil. A small plastic case attached to the rear body has two packets where the spring loaded carbon brushes are placed inside each pocket. The spring is needed to maintain a tight contact of the brush with the slip ring during the operating. Carbon has low friction and good conductivity, which causes less harmonic distortion and low power consumption, respectively. A stranded copper wire is embedded at the bottom end of each brush. The wire is extended with a longer 12AWG wire, which is linked to an external power supply.

f. Sheave and Fan

A 2-1/4" diameter sheave and a 18 bladed main fan are mounted at the front end of the rotor. The sheave has a 5/8" bore and a deep V groove matched with a 3VX V belt. The main fan cools down the entire generator by ventilating air over the outside surfaces as well as through the inside pores. Since the sheave bore and the fan bore do not tightly fit with the shaft, there exists great possibility of rotor unbalance, which often causes dynamic eccentricity [1]. Moreover, the originally wrapped blades due

to poor quality control can be another source of dynamic eccentricity. This problem occurs in practice and no remedy is studied in this research.

#### g. Bearings

Two ball bearings are mounted at both ends of the shaft for rotor support. The front bearing is a 6203-2RS type ball bearing and the rear bearing is a smaller 6200-2RS type. The original equipped front bearing is a KBC 6203-2RS type. However, an ORS 6203 type is chosen due to the easy availability of this bearing in the market. The ORS 6203 bearing type is consistently used through the whole experiments.

The front bearing can be easily disassembled from the shaft, however, the disassembly of the rear bearing without damaging the slip rings is found to be very difficult. The disassembly and reassembly process of a bearing is inevitable in this research. Hence, only the front bearing is damaged in the experiments.

The front bearing is equipped with two rubber shields. An embedded steel washer internally supports the rubber shield. The outer circumference of the shield tightly fits into the outer ring so that the rubber shield does not rotate while the inner ring rotates. The rubber shield bore is featured with a thinner and softer rubber seal. The soft seal barely contacts the inner ring so that it does not cause excessive friction or heat when proper lubrication is applied on. During the experimental preparatory process, the rubber shields are removed using a tiny flat headed screw driver in order to access the bearing grease. Improper disassembly of the shields is found to cause the embedded supporting washer to wrap. Then the wrapped washer causes irregular contact of the seal with the inner ring and later burning marks on the contact points.

Bearing grease fill percentage varies from manufacturer to manufacturer [31]. Generally speaking, about 40% of the inside empty volume is occupied by bearing grease. Stack *et al.* have proposed to use a 3 to 5% grease fill in order to accelerate

bearing damage while minimizing the effects of reduced grease fill percentage [31]. It is observed that using 5% grease fill in ORS 6203 type bearing accelerates the bearing damage process during the test runs.

#### h. Front and Rear Body Units

The front and rear generator body units look like a hollow cylinder with one open side. They are made of soft steel alloy. Both have the same diameter, but the rear body unit has longer length. The circumferential groove on the open end of the body unit tightly fits with the matching groove in the stator upon assembly. There exist gaps between the three front radial columns that connect to the bearing housing at the closed end of the front body unit. The closed side of the rear body unit is porous. The gaps and holes at the closed ends form air pathways. The front bearing housing is slightly extruded from the closed end of the front body unit. This feature is important since unwanted proximity to the stator magnetic field causes higher magnetic flux density on the outer ring surfaces, which can cause premature bearing failure [37]. The rear body unit also has a bearing housing for a smaller 6200 type bearing. There exist an original plastic electric insulator inside of the rear bearing housing since a shaft voltage always exists in electrical machines as a result of asymmetry of faults, air-gap fields, magnetized shaft, asymmetry of the magnetic fields, electrostatic effects and so on [29], [38]. This electric insulator is the key component that blocks a normally induced shaft current as well as the externally injected bearing damage current to flow through the rear bearing and form a current loop.

The improper assembly and disassembly processes of the body units and the front bearing can cause misalignment problems. Four types of typical misalignment of bearings are depicted in Fig. 5. Since the front bearing housing is made of soft steel, it can be easily deformed if a large force is applied during the bearing disas-

sembly process. The deformed bearing housing can cause the most common type of misalignment called the tilted race [9]. Three long bolts tighten the front body unit, the stator body, and the rear body unit together. The bolts are evenly spaced on the circumferences of the bodies by 120 degrees. Over-tightening one of the bolts can cause the front and rear body units to be off-centered, hence resulting in the out-of-line misalignment and the tilted race misalignment. A torque wrench is used to set a proper torque consistently throughout the experiments.

## 2. The Induction Motor and AC Motor Drive

The common mechanical power sources in power generation systems are obtained from fossil energy, hydro potential energy, and wind energy. The mechanical equipment that harnesses the above-mentioned energy sources typically occupy very large space, which is unsuitable for a typical laboratory environment. Moreover, operating such equipment requires highly complex skills and special knowledge that are often difficult to obtain in a short research period. Due to these difficulties and the availability of 3HP induction motors and AC motor drives in the research lab, a 3HP induction motor is chosen as the mechanical power source prime mover to the synchronous generator.

The required power rating of the induction motor is estimated based on the typical energy efficiency of Lundell alternators based on [36], estimated energy loss due to soft coupling, and the estimated motor torques that match the required generator torques at the operating frequencies based on [36], and the performance test results of the induction motor.

The 3HP induction motor is driven by a Delta VFB-B series 3HP AC motor drive. The inverter can drive the motor at up to 3600 rpm and the motor speed can be set by the inverter. It is noted that no speed control loop is used in the motor.

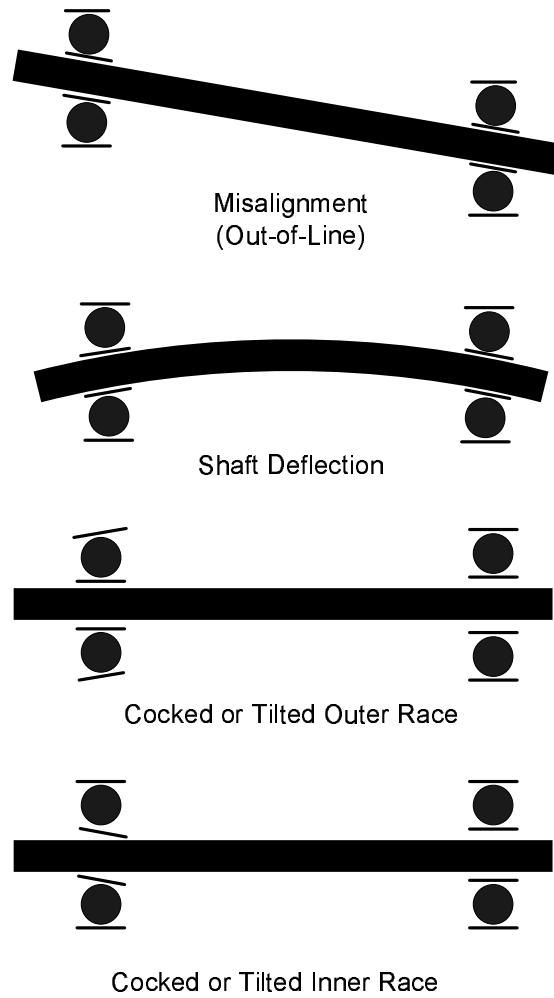


Fig. 5. Four types of ball bearing misalignment [9].

The induction motor is tightly bolted on the 1" steel plate. Therefore, a high amount of bearing damage current due to the *in-situ* bearing damaging process can flow through the motor chassis, the inverter, and the connected power distribution lines. The grounding connection to the induction motor chassis is disconnected in order to protect the inverter circuit and the rest of the electrical equipment that might be harmed due to this current. The removal of the grounding connection also avoids forming a grounding loop thorough the returning line of the *in-situ* bearing damage circuit.

A driving sheave is mounted on the rotor of the induction motor. The driving sheave is of the same size as the driven sheave in the generator. The two sheaves are connected via a 3VX V belt. Hence, the speed ratio of the two sheaves is about 1 to 1.

### 3. The V Belt

The V belt plays an important role in transferring the mechanical power to the generator from the induction motor. The selection of the 3VX belt is based on that the 3VX belt has the required power transmission rating and the deep V groove that matches with the one of the driven sheaves. The matching driving sheave is chosen later. In addition, one of the advantages of using a V belt instead of a serpentine belt is that the sheave alignment process is relatively permissive [36].

The V belt has a 45" circumferential length and the inner cogged wedges that provide uniform bending stress distribution according to the manufacture's claim. It has a trapezoidal cross section. The mismatch between the deep V groove of the sheaves and the cross section of the belt often causes excessive heat generation and increased rotor vibration [36].

The required belt tension is measured with the simple deflection method based

on the standard belt manufacture's recommendation. The correct tension can be set when the belt deflection caused by a down-force of 3.9 to 4.8 lbs at the belt mid-span is equal to the length of the belt span multiplied by  $1/64$ ". The belt span is the distance between the centers of the sheaves and it is about 22". Hence, the correct deflection is  $22/64$ ".

#### 4. Miscellaneous Mechanical Parts

The 1" thick steel plate is mounted on a steel moving cart. It serves as a mounting foundation for the generator, the induction motor, and the other mechanical components.

A belt tension adjuster is mounted on the steel plate. This adjuster consists of a mounting bracket and a curved extension bar with a  $3/8$ " bore and a 4" long wide slot with a  $3/8$ " bore. The bracket is mounted in the middle of the steel plate. The extension bar is connected to the mounting bracket through a  $3/8$ " stud bolt and a nut, The bar can rotate around the connecting point. The sliding slot in the extension bar is connected to the upper mount of the front body unit through a  $3/8$ " bolt. The front body unit also has a lower mount at the bottom and the lower mount is connected to a generator mounting bracket through a  $1/2$ " bolt and a nut. The generator bracket is sturdily mounted on the steel base. Therefore, the generator can rotate around the lower mounting point. Relocating the upper mount connecting position along the sliding slot can result in tension adjustment.

The moving car itself weighs more than 100 lbs. The additional weights of the steel plate and safety glass at the sides increase the total weight of the cart. This heavy weight foundation functions as a vibration absorber.

## 5. The Field Excitation Power Supply

The rotor field is energized by an external power supply. Since the voltage regulator and the 3- $\phi$  rectifier are removed, a field excitation DC current fed to the rotor coil is provided by an external power supply.

An Agilent HP E3631A power supply is chosen due to its availability in the laboratory. It can provide up to 5A DC within 0 to 6V. In addition, the power supply is powered by a 1- $\phi$ , 120V power line from a standard power outlet, while the *in-situ* bearing damage circuit uses separate industrial power lines. Therefore, the high current used to damage the bearing does not affect the proper operation of the power supply.

## 6. The Electrical Load

This generator produces a 3- $\phi$  AC power and the output power is consumed by a bank of three resistors. The electrical load consists of three OHMITE D225-ND power resistors, a piece of wooden plate, and low resistivity stranded 8AWG wires. Each of the power resistor has a 225W power rating and a  $5\Omega$  resistance. Hence the maximum current that the power resistor can carry is about 6.7A. The required power rating is initially estimated based on the test results of the alternator. The resistors are mounted on the wooden plate, which also serves as a heat insulator. The resistors are wired to form a delta winding. The three terminal connections of the delta winding are connected to the three armature terminals.

The maximum power output of the generator is tested when the generator is driven at 60 Hz and the field current is set to 2A DC. The maximum phase voltage is about 16V AC rms and the maximum line current is about 5.5A AC rms. This output power is consumed by the electrical load. The output power is calculated based on



the following equation.

$$P = \sqrt{3}V_{phase}I_{line} \quad (2.1)$$

where  $V_{phase}$  is the phase voltage,  $I_{line}$  is the line current. The maximum power consumption of the electrical load is about 150W.

### C. Sensors and Data Acquisition Systems

The three armature line currents, the two armature phase voltages, the field current and the field voltage, and lastly the three accelerations are measured and collected in this research. Each section discusses the required equipment for each of the above mentioned measurements. The circuitry of the entire electrical system including the sensors and the bearing damage circuit is depicted in Fig 6.

#### 1. Armature Voltage Sensors

The armature phase voltage sensing equipment consists of a Flex-Core 2VT469-120 potential transformer (PT) and two sets of  $1M\Omega$  and  $150K\Omega$ , 1% precision resistors. The PT consists of two 1- $\phi$  PT's with the 1:1 turn ratio and the 99.7% measurement accuracy. It is configured to form an open delta winding by connecting two primary side terminals from each of the 1- $\phi$  PT's. The three terminals from the primary side are linked to the three armature terminals via three 18AWG wires. The wires are denoted by A, B, and C in Fig. 6. On the secondary side, two terminals are connected in the same manner as the primary side and then the connection terminal is electrically grounded through a 120V standard power outlet. The voltage across the ungrounded secondary side terminal and the grounded terminal is measured. After trial and error, it is found the voltage measurement at the secondary side of the PT

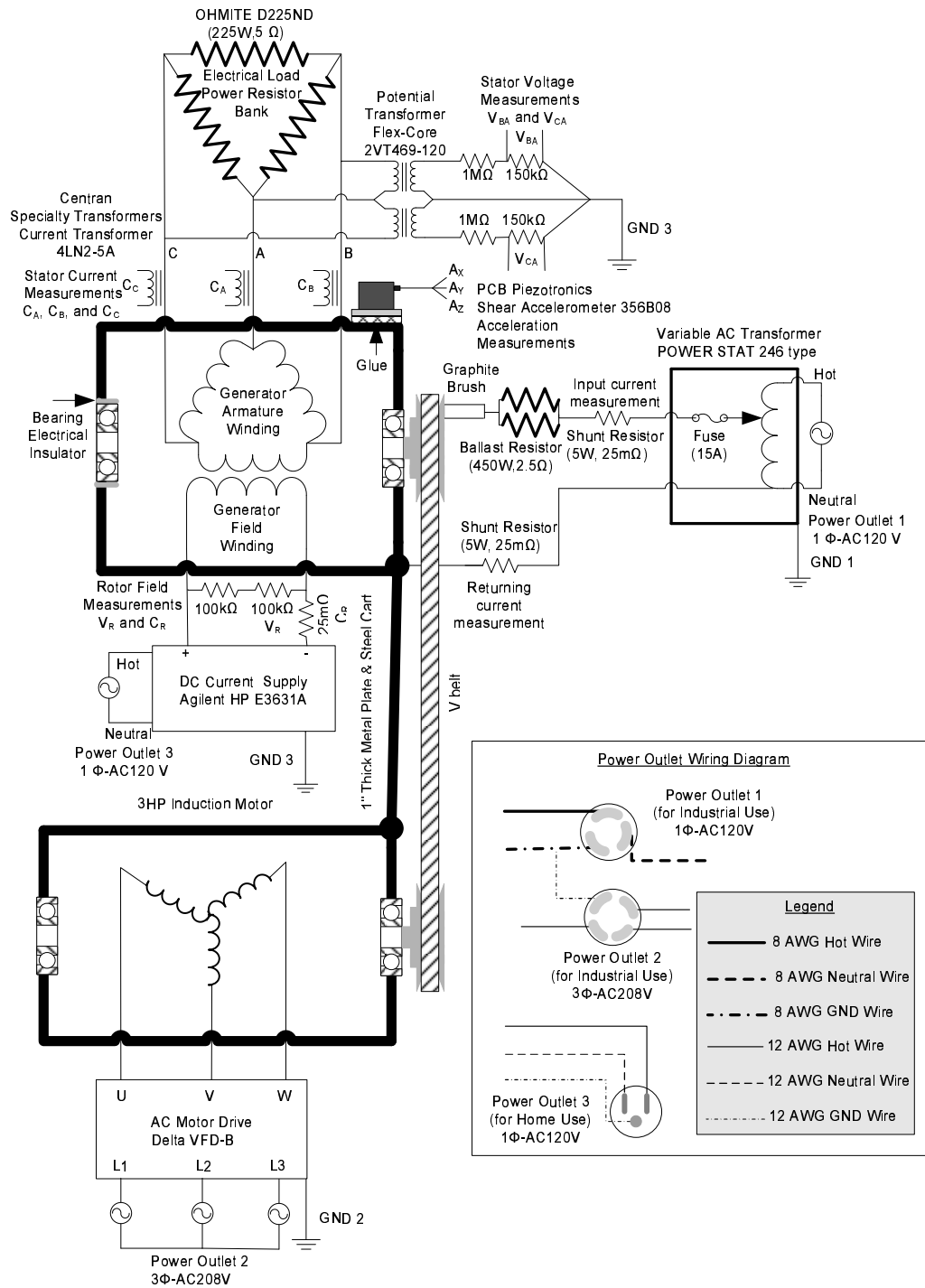


Fig. 6. Circuit diagram of the whole electrical systems.

exceeds 5V, which is the maximum voltage input of the NI DAQ. Therefore, a pair of voltage dividers are installed to step down the voltage measurements. The voltage divider consists of a  $1\text{M}\Omega$  and a  $150\text{K}\Omega$  precision resistors. Hence the voltage step-down scale is 3 to 20. The measured phase voltages are denoted by  $V_{BA}$  and  $V_{CA}$  in Fig. 6.

## 2. Armature Current Sensors

Three Centran Specialty Transformers 4LN2-5A current transformer (CT) sense the three line currents,  $C_A$ ,  $C_B$ , and  $C_C$  that pass between the armature and the electrical load. Each power wire runs through the closed core of a CT, and the CT senses the line current passing through the inside core. This CT has a conversion ratio of 330 mV AC output voltage per 5A AC input current and 99% accuracy.

## 3. Field Voltage and Current Sensors

The voltage across the field coil terminals and the field current passing through the coil are measured by using a voltage divider and a shunt resistor, respectively. By trial and error, it is found that the field voltage exceeds the maximum input voltage of the NI DAQ. Therefore, the voltage divider is installed to step down the field voltage. The voltage divider consists of two  $100\text{K}\Omega$ , 1% precision resistors. A  $25\text{m}\Omega$ , 1% precision shunt resistor is installed in the returning current path.

## 4. Vibration Sensor

A PIEZOTRONICS three axis shear accelerometer is used for rotor vibration sensing. This accelerometer is capable of measuring  $\pm 50$  peak gravitational acceleration (G) with the sensitivity of 100 mV/G from 0.2 Hz up to 5000 Hz. It is mounted on the left side of the front body unit as depicted in Fig. 1. The location of the accelerometer is

chosen considering that the induced bearing faults are expected to be initiated from the high loading zone due to the belt tension.

## 5. Data Acquisition Hardware

The data acquisition hardware consists of a NI PCI-6070E DAQ card, a NI SCXI-1531 8 channel accelerometer input module, a NI SCXI-1141 8 channel low pass filter module, and a SCXI-1305 AC/DC coupling BNC terminal block. The DAQ card has a capability of sampling 16 channel of analog inputs with 16 bit resolution. The sampling mode is set to be a multiplexed mode. The accelerometer input module has a built-in 4-pole Bessel low pass filters whose bandwidth is set to 5000 Hz, the same as the bandwidth of the accelerometer. The SCXI-1141 low pass filter module has built-in 8th order elliptical filter whose cutoff frequency are automatically set by the DAQ card. Low pass filtering is required to avoid aliasing. The BNC terminal block is plugged into the NI SCXI 1141 module. The BNC terminal block has 8 single pole high pass analog filters with a cutoff frequency of 0.16 Hz. The high pass filters can be disabled channel by channel. The input signals connected to the BNC terminal block can bypass the high pass filters when external grounding connections are not required for them. The CT outputs require these external grounding connections since the output signals are floating. The physical channel allocation is summarized in Table I.

## 6. Data Acquisition Software

A VI program that runs under the NI LabView Version 6.1.4 saves the 7 or 10 channels of the experimental measurements into data files. It has 5 editor boxes in which the sampling rate, the total number of sampling points, the total number of files, the delay time, and the file name can be typed in. The time delay function allows to collect

the experimental data and save a file every specified time interval. A flowchart of the data acquisition algorithm is depicted in Fig. 7.

Table I. NI DAQ channel allocation.

Assigned		Designated	
Program	Module	Physical	Description
Channel Number		Channel Number	
0	NI SCXI 1531	0	Acceleration X Axis
1	NI SCXI 1531	1	Acceleration Y Axis
2	NI SCXI 1531	2	Acceleration Z Axis
3	NI SCXI 1141	0	Armature Voltage BA
4	NI SCXI 1141	1	Armature Voltage CA
5	NI SCXI 1141	2	Field Voltage
6	NI SCXI 1141	3	Field Current
7	NI SCXI 1141/1305	4	Armature Current A
8	NI SCXI 1141/1305	5	Armature Current B
9	NI SCXI 1141/1305	6	Armature Current C

In addition, the channel allocation in this program is different from the physical channel allocations. The program channel allocation is summarized in Table I.

#### D. *In-situ* Bearing Damage Device

The *in-situ* bearing damage method presented in [29], [38] is adopted to damage the front ball bearing *in-situ* during an experiment. During the bearing damage process, a large amount of AC current is externally injected across the inner and the

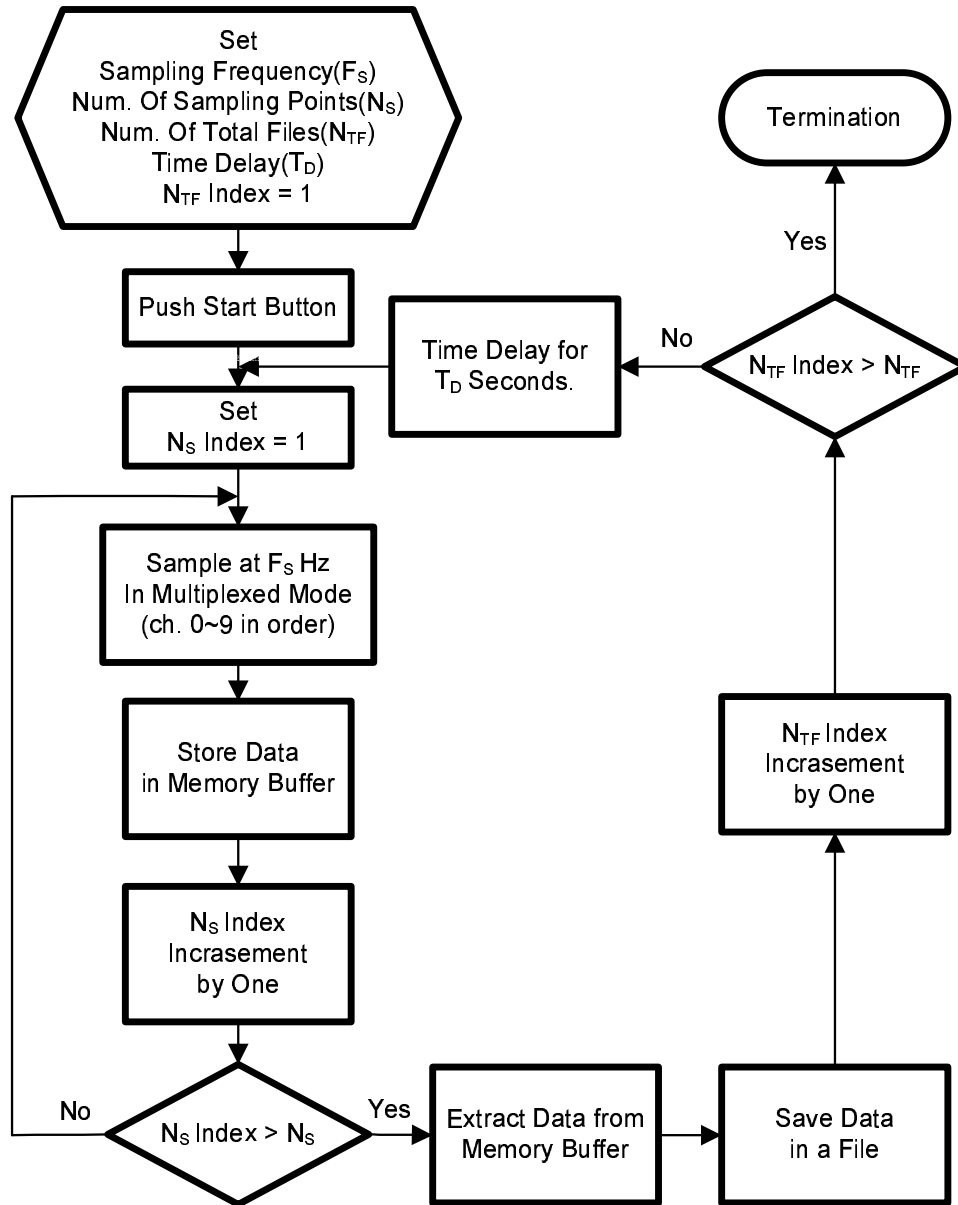


Fig. 7. Flowchart of data acquisition algorithm.

outer races of the bearing. The detailed bearing failure mechanism of this method is described in the next section. The key components of the bearing damage device include a variable AC transformer, two power resistors, two shunt resistors, and a carbon brush as shown in Fig 8. More information on each component is described below.

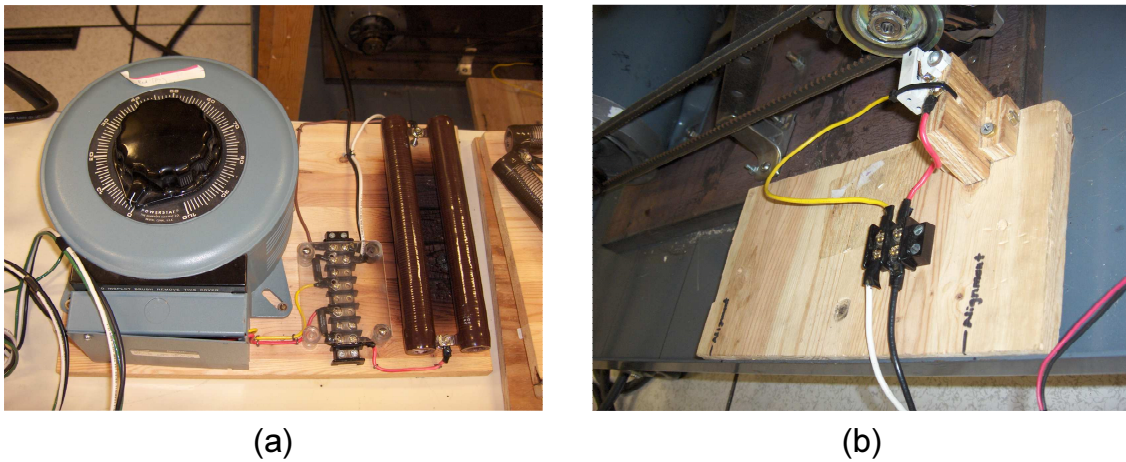


Fig. 8. Picture of the bearing damage device, (a) current injection circuit (b) bearing damage carbon brush.

#### 1. Mechanism of Rolling Element Bearing Failure due to Shaft Current

The failure mechanism of rolling element bearings is presented in [31], [32], [33], [34], [38]. There are two kinds of bearing grease and each type causes a different bearing failure mechanism due to its different resistivity.

The first kind is low resistivity bearing grease. It has less than  $10^5 \Omega\text{-m}$  volume resistance. When a shaft current exceeds a threshold, a silent discharge occurs through the inner race, the rolling elements, and the outer race. This leads to decomposition of the bearing grease and then corrosion on the surfaces of the raceways. In loaded

areas or on the corroded surfaces, increased erosion, surface softening, and plastic deformation occur, finally resulting in mass transfers and high local temperatures on asperities of the friction surfaces. These cause the bearing fatigue life to decrease, which is evidenced by the formation of corrugations, and finally bearing failure.

The other kind of bearing grease is high resistivity grease which has a volume resistance of more than  $10^9 \Omega\text{-m}$ . When high resistivity grease is used, the grease film acts as a capacitor and causes the accumulation of electric charges. A sudden burst of the charges occurs when the race to ball asperity contacts get close, which generates large discharge currents. This causes electric arcs, high local temperatures, and molten pits. The pits are prone to advance a fluting. As the bearing degradation advances, more flutes appear throughout the raceways and this leads to bearing failure.

## 2. Variable AC Transformer

A POWERSTAT 246 type variable transformer is chosen due to the availability in the laboratory. The output current is controlled by a top knob. The maximum output current is 15A, which exceeds the maximum current used in [31]. It has a built-in 15A safety fuse. This transformer is energized by 1- $\phi$ , 125V power lines from an industrial power outlet. The other equipment are not powered through this power outlet due to a large bearing damage current. For safety, the ground wire from the power outlet is connected to the transformer chassis.

## 3. Power Resistors and Shunt Resistors

Two OHMITE 225W,  $5\Omega$  power resistors are connected in parallel and they function as a 450W ballast resistor that stabilizes the bearing damage current. Two 5W,  $25\text{m}\Omega$ , 1% precision resistors are mounted in the hot and the neutral wires, respectively. The



shunt resistors are used to measure the input current and the returning current. The connection diagram is depicted in 6.

The maximum allowable current of the bearing damage circuit is 13.4A due to the maximum carrying current of the ballast resistor. It is noted that this maximum current still exceeds the current used in [31].

#### 4. Carbon Brush

A carbon brush can deliver high current while imposing little friction. Hence it can be a good solution for this application.

A spring loaded carbon brush is used to connect the hot wire of the bearing damage circuit to the rotor shaft. The carbon brush is placed in a plastic case and the case is mounted on a wooden support. Upon the installation of the wooden support on the cart, the loaded spring pushes the carbon brush towards the driven sheave and the carbon brush contacts with the sheave on the side. The hot wire from the variable transformer is connected to the carbon brush. The bearing damage current can flow through the carbon brush to the driven sheave, the main shaft, and then the front bearing. The return wire is connected to the lower mount of the front body unit. The current passes through the inside the bearing and returns to the neutral wire. The connection diagram is depicted in Fig 9.

Mounting of the carbon brush presents a problem. During a test run, it is observed that the carbon brush is prone to bounce abruptly as the sheave rotates and the abrupt movement of the carbon brush sometimes causes sparks at the contact point. This may be related with the fact that the side surface of the driven sheave is not polished. This may cause unwanted mechanical disturbances and distort output signatures. A detailed description of this problem is depicted in Fig. 10. The following remedies are made as follows: A plastic case is placed very close to the sheave so that

most of the carbon brush stays inside the case. This ensures that the yaw and pitch angles are smaller. In addition, a small piece of vinyl sheet is inserted in the plastic case to minimize the lateral free movement of the brush. After this remedy is applied, it is observed that the bouncing movement is minimized and the carbon brush moves forwards smoothly as it wears out during a long experiment.

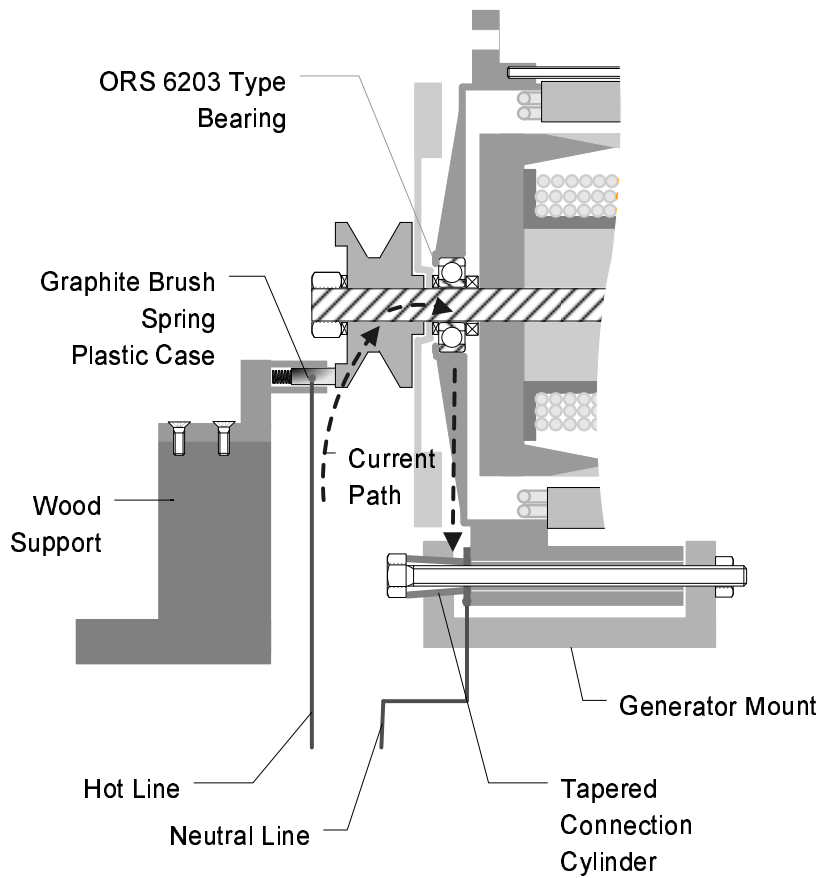


Fig. 9. *In-situ* bearing damage circuit installation and shaft current path.

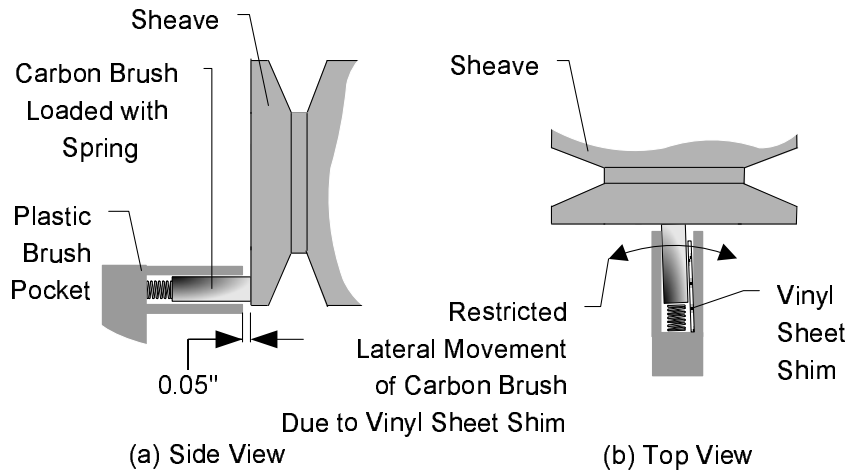


Fig. 10. Carbon brush installation issues.

## E. Chapter Summary

This chapter gives an overview of the experimental setup used in this research. The experimental equipment is scrutinized in terms of the design viewpoints, the operating principles, and the dimensions with the aid of diagrams. Some assembly and installation issues are addressed and the remedies are provided. The specifications of the DAQ hardware and sensors are addressed and the parameter settings of the DAQ hardware and other electrical equipment are described.

## CHAPTER III

### DESCRIPTION OF THE EXPERIMENTAL PROCEDURES

#### A. Introduction

An overview of experimental setup is described in the previous chapter. This chapter discusses the experimental procedures in this research. This chapter is largely divided into two sections. The first section elaborates on the experimental preparation, and the second section discusses the experimental execution in detail.

#### B. Preparation for the Experiments

This section discusses the experimental preparation. This preparatory process includes the proper installation of the key mechanical components, the reconditioning process of the front bearing, and the parameter settings in the experimental equipment.

The front bearing is reconditioned in order to accelerate the bearing damage process. The synchronous generator is the major component in this experiment. The previous chapter discusses the adversary effects of improper assembly and installation. Detailed processes to avoid those problems are also discussed. Based on these guidelines, detailed reassembly, reinstallation, and alignment procedures are also discussed. Finally, parameter settings regarding generator operation are discussed.

##### 1. Bearing Reconditioning and Installation

The main purpose of the front bearing reconditioning process is to control the bearing grease fill percentage in order to expedite the bearing damage process. In [38], the experimental results show that with the original amount of bearing grease, it takes

more than 250 hours to damage a NU326 bearing using 50A of current. Hence, the disadvantages of using an original grease fill percentage include very long experimental time and a dangerously high current.

Stack *and et al.* claim that the bearing grease fill percentage is one of the main factors that determines bearing failure time under the influence of an electrical current [31]. In the paper, a 6205 type bearing with only 3 to 5% grease fill is fully damaged within 8 to 36 hours using 0.4A to 12A of bearing current. The effects of the reduced bearing grease fill on the bearing failure time is also discussed in the same reference; the experimental results show it takes about 125 days to damage the same bearing under normal operating conditions without injecting any bearing current.

The bearing reconditioning process begins with the disassembly of the two shields in a 6203 bearing. The black rubber shield is fortified with an inside metal ring. The ring can be bent easily during the removal. It is noted that the bent ring can contact with the bearing train sporadically during the running, and cause unwanted mechanical disturbances. The removal procedure is described in the previous chapter. After the removal, some amount of the original bearing grease is scooped out and then preserved in a small container for later use. The remaining bearing grease in the bearing is removed as much as possible and the bearing is soaked in degreasing solvent. The first degreasing process removes most of the bearing grease left inside the bearing. The second degreasing process is required to clean the bearing thoroughly. Then the bearing is dried in the open air for an hour to allow evaporation of the solvent in the bearing.

The empty volume of a 6203 type bearing is measured in order to decide the amount of repacking grease. The empty volume is the space between the inner and outer rings excluding the balls and the train. In the measurement process, solvent in a syringe is dropped into the bearing with one shield airtight until the solvent starts

to overflow over the edges of the bearing. The total volume change in the syringe is the empty volume of the bearing. Repeating the above procedures gives an average empty volume of 2ml.

Approximately 5% of the bearing empty volume is repacked with the preserved original bearing grease. The amount of repacking bearing grease is measured in a small 0.1ml container. Since the amount of repacking grease is very small and the measurement is quite difficult, there is some variation in this amount. The grease is put on all over the inner and outer raceways using a tiny non-metallic stick in order not to scratch the surfaces. It is noted that there exists a variation on the distribution of the bearing grease inside the bearing since the uniform distribution is impossible. After the repacking procedure, the other shield is closed carefully.

A three legged bearing puller is used to remove the front bearing from the bearing housing. The three legs hold the bearing housing and the pulling screw pushes the inner ring against the bearing housing. Since the bearing housing is made of soft steel alloy, an unbalanced pulling can cause damage to the housing. Therefore, careful attention is paid during the execution of this procedure.

The front bearing installation does not require any specialty tool. Pushing the outer race sequentially clockwise or counter clockwise against the bearing housing advances the bearing into the housing. If installed properly, there is an even gap between the tapered edges of the outer race and the housing. In order to prevent false brinelling on the raceways, the inner race is never pushed.

## 2. Generator Assembly, Mounting, Belt Tension Adjustment and Alignment

The three body assembly bolts tighten the front body, the rear body, and the stator core. The three bolts are tightened using a torque wrench with a consistent 7.5 lb-ft torque in order to avoid the misalignment discussed in the previous chapter.

The bottom mounting point is connected to the generator mounting bracket that is firmly installed on the 1" steel foundation. The top mounting point is attached to the belt tension adjustment bar. If the connections get loose due to high vibration and a long time of operation, this also causes the sheaves to be out of alignment and the belt tension to vary during the experiment. Therefore, the 3/8" bolts in the mounting points are firmly tightened using a torque wrench with a 20 lb-ft torque, which is a typical amount of torque for an alternator installation.

After the body mounting, the belt tension is set according to the manufacture instructions as follows: Using the thumb, a few pounds of force is applied in the middle of the belt span. The deflection of the middle point is 22/64", if correctly set. After each trial, the location of the upper mounting bolt is marked on the slot in the belt tension adjustment bar. After a few trials for averaging, it is found that the marked locations vary by about 3/8". In order to minimize the effect due to a varying belt tension, a single point in the varying range is selected to set an equal tension throughout the experiments.

The sheave alignment causes another challenge. If the two sheaves are properly installed, the two are placed in a single place and the two sheave axes are in parallel. If the axes are slightly off parallel, it is observed that noticeable belt vibration appears. This introduces mechanical disturbances to the system. By tinkering with the tapered cylinder in the lower mounting bracket, the belt vibration can be subdued. By trial and error, a proper position of the tapered cylinder is set, which reduces belt vibration and overall startup machine vibration.

### 3. Field Current

The field excitation current is set to 2A DC throughout the experiments. The rotor field coil is connected to an Agilent HP E3631A power supply via 12AWG wires. The

Agilent power supply has two sets of power terminals. The first set can provide 1A DC within  $\pm 25V$  and the second set can deliver 5A DC within 0 to 6V. Since a typical amount of field excitation current in automotive alternators reaches up to about 10A DC [36], 5A DC is still within the maximum current range. By trial and error, it is found that injecting 2A DC of field current produces about a 5.5V voltage drop across the terminals. Hence, the maximum current this power supply can provide is 2A DC and this amount of field current is consistently set throughout the experiments.

#### 4. Bearing Damage Current Magnitude

The bearing damage circuit can provide up to 13.5A of current. Since a large amount of current is dealt with, the leakage current may damage other systems such as the induction motor and the sensors. To ensure all the injecting current returns to the neutral line, a test is performed as follows: A small amount of current is injected first and the amounts of injecting and returning currents are measured using the shunt resistors in the circuit. It is found that all the injecting current returns to the neutral line. The process is repeated while the amount of injected current is increased. Finally, it is confirmed that 13 amps of current can be injected without causing any problems to the other components.

In the bearing failure mode of this research, the bearing failure time depends on the injecting current density, which is the ratio of the injecting current to the contact area [33]. The contact area is affected by many factors such as the amount of loading, the sheave alignment, and so on. Therefore, it is difficult to control the contact area. Setting the same amount of injected current reduces the possibility for high variation on the current density.

A test experiment is performed in order to set the magnitude of the bearing damage current. The results show that it takes about a day to fully damage the



6203 bearing with about 5% grease fill using 12A of current from the *in-situ* bearing damage circuit. The current magnitude is set to 12A AC throughout the experiments.

### 5. Parameter Settings in the Data Acquisition Program

The sampling frequency,  $F_S$ , is set to 7680 Hz. Given that the rotor has six pole pairs, the electrical fundamental frequencies are about 240 Hz and 120 Hz at the mechanical rotational speeds of 40 Hz and 20 Hz, respectively. The Nyquist frequency is 3840 Hz, therefore, the sampling bandwidth adequately covers up to about the 16th harmonic for the 40 Hz case and the 32nd harmonic for the 20 Hz case. Therefore, if the mechanical frequencies are modulated by the large harmonics such as the fundamental and the fifth harmonics, these will still be in the Nyquist frequency range.

The number of sampling points per a file is set to 230,400, which accounts for 30 seconds of data acquisition time at  $F_S=7680$  Hz. The sampling resolution is, therefore, about 0.033 Hz. After examining the output signatures, the frequency resolution is found to be adequate for this research.

When the 7 channels of experimental data is collected during the test experiments, it is found that it takes about 40 seconds to save a file at the sampling frequency of 7840 Hz and the sampling time of 30 seconds. The single file size is about 21M bytes. The total file archive size becomes typically in the range of 10s of Giga bytes. The large amount of data causes a storage problem and also increases a computational burden during the data processing. In order to ease some of the computational burden, a time delay is inserted to the DAQ process so that the file are saved every 5 minutes.

### C. Execution of the Experiments

The experimental plan consists of two case studies and they are explained in detail. Each experiment period is divided into three sub periods: the pre-running period, the healthy baseline DAQ period, and the DAQ period with the *in-situ* bearing damage process on. The detailed timetable is explained below.

#### 1. Setting of the Different Operating Conditions

Several case studies regarding to the bearing fault detection of an induction motor with different operating conditions are presented in [25]. The results show that the bearing fault detection capability varies as the operating conditions change. Therefore, it is worth to examine the bearing fault detection capability of the developed indicator in this research with different operating conditions.

Two case studies are examined in this research. In the first case study, the inverter frequency is set to 20 Hz. The inverter frequency setting for the second case study is 40 Hz. Accordingly, the generator mechanical speeds are approximately 20 Hz and 40 Hz, respectively.

The rotational speed setting in the case studies explored are based on the normal operating speeds of small synchronous generators. The mechanical rotational speed of a synchronous generator largely depends on the type of the input mechanical power source [35]. For example, a typical small synchronous generator powered by a diesel engine has a 4 pole rotor and runs at 30 Hz since an engine runs most efficiently around 2000 rpm and the power line frequency is 50 or 60 Hz. The mechanical rotational speed is calculated based on the electrical output frequency and the number of rotor poles as follows:

$$f_{mechanical} = \frac{2 \times f_{electrical}}{N_{pole}} \quad (3.1)$$

where  $f_{mechanical}$  is the mechanical speed in Hz,  $f_{electrical}$  is the electrical speed in Hz, and  $N_{pole}$  is the number of rotor poles. Given that the typical frequency of power lines is 50 or 60 Hz and a small synchronous generator has 4 poles, the mechanical speed of a synchronous generator ranges from 25 Hz to 30 Hz. Therefore, the 20 Hz and 40 Hz generator mechanical speeds are close to this frequency range, and the difference in the mechanical frequency can provide quite different operating conditions to test the concepts of this research.

The operating speed change also causes the electrical loading change. When the generator runs twice as fast, the armature EMF is doubled and the output current and voltage are also increased according to the load impedance. So is the power consumption in the electrical load. Therefore, the different generator rotational speed settings provide vastly different operation conditions due to the electrical loading change, in addition to the speed change.

## 2. Experimental Plan Table

The experiments are divided into two groups: the 20 Hz group and the 40 Hz group. Each group consists of five experiments in order to investigate the repeatability of the results.

The experiments are organized randomly. Throughout the experiments, the grease fill percentage and the amount of bearing damage current remain constant. In the first five experiments, the vibration data were not collected because the vibration sensor was not mounted due to concern that the high current used to damage the bearing may damage the sensor. The detailed experiment plan is summarized in Table II.

Table II. Summary of experimental plan and parameter settings.

Exp. Order	Group	Injected Current (A)	Grease Fill (%)	DAQ signals
1	40 Hz	12	5	armature & field
2	40 Hz	12	5	armature & field
3	40 Hz	12	5	armature & field
4	20 Hz	12	5	armature & field
5	20 Hz	12	5	armature & field
6	20 Hz	12	5	armature & field & vibration
7	20 Hz	12	5	armature & field & vibration
8	40 Hz	12	5	armature & field & vibration
9	40 Hz	12	5	armature & field & vibration
10	20 Hz	12	5	armature & field & vibration

### 3. Experimental Timetable

The generator is driven for an hour before the data acquisition process starts. The purpose of the pre-running period is to drive the generator system into thermal equilibrium before the data acquisition process begins. During the pre-running, the belt tension builds up, and the bearing grease forms adequate films between the raceways and the balls. All the electrical components like the electrical load reach thermal stability as well. Meanwhile, the sheave alignments and the position adjustment of the carbon brush mount are performed manually.

After the pre-running, the LabView program used in data acquisition is started and used to store experimental data into files. During this period, no external current

is injected through the shaft. Therefore, the front bearing is considered to be healthy. The DAQ process lasts for 4 hours. The purpose of this period is to collect baseline data with which the baseline healthy indicators are calculated. This period ends when the *in-situ* bearing damage process starts while the DAQ program continues to run.

As soon as the healthy period ends, the *in-situ* bearing damage circuit is switched on. The magnitude of the bearing damage current is slowly increased by rotating the control knob of the variable AC transformer clockwise. The current amount is repeatedly monitored using the shunt resistors in the circuit. When the current reaches 12A, the current level is held at that level for 10 minutes or so. It is often observed that the bearing damage current level drops by a fraction of an Amp. Then the current level is calibrated to 12A. As the bearing damage process advances, the front bearing exhibits signs of deterioration such as increasing noise and rotor vibration. When the bearing makes excessive noise or rotor vibration, the experiment is terminated by switching off both the damage circuit and the AC motor drive.

#### D. Chapter Summary

This chapter discusses the experimental procedures. First, the experimental preparatory procedures are explained in detail. The experimental plan is presented with the details of two case studies performed. Finally, the detailed experimental timetable is described.

## CHAPTER IV

DIGITAL SIGNAL PROCESSING OF EXPERIMENTAL DATA AND ANALYSIS  
OF RESULTS

## A. Introduction

The experimental plan is discussed in the previous chapter, and the experiments are accordingly conducted. This chapter discusses the data analysis. In the first section, the data processing routines are described in detail. In the second section, the results are presented after the data processing process. In addition, a signal refers to a digitally sampled signal in the rest of the thesis.

## B. Data Processing Routines

The terminal armature voltage and current of the synchronous generator can be described in a simplified lumped model as follow [35] :

$$\mathbf{V} = \mathbf{E} - \mathbf{I} \cdot (\mathbf{Z}_S + \mathbf{Z}_L) \quad (4.1)$$

where  $\mathbf{V}$  is the terminal armature voltage,  $\mathbf{I}$  is the terminal armature current,  $\mathbf{E}$  is the armature EMF due to field flux,  $\mathbf{Z}_S$  is the synchronous machine impedance, and  $\mathbf{Z}_L$  is the load impedance. Hence, whatever changes occur in the armature EMF due to the bearing faults, these will show up in the armature voltage.

The health indicator used in this research is calculated based on the armature line voltage measurements as this variable forms the generator output. The data processing program consists of three sequential routines: the pre-processing routine, the main processing routine, and the post-processing routine. A flow chart of these routines is depicted in Fig. 11. The data processing routines are written in Matlab.

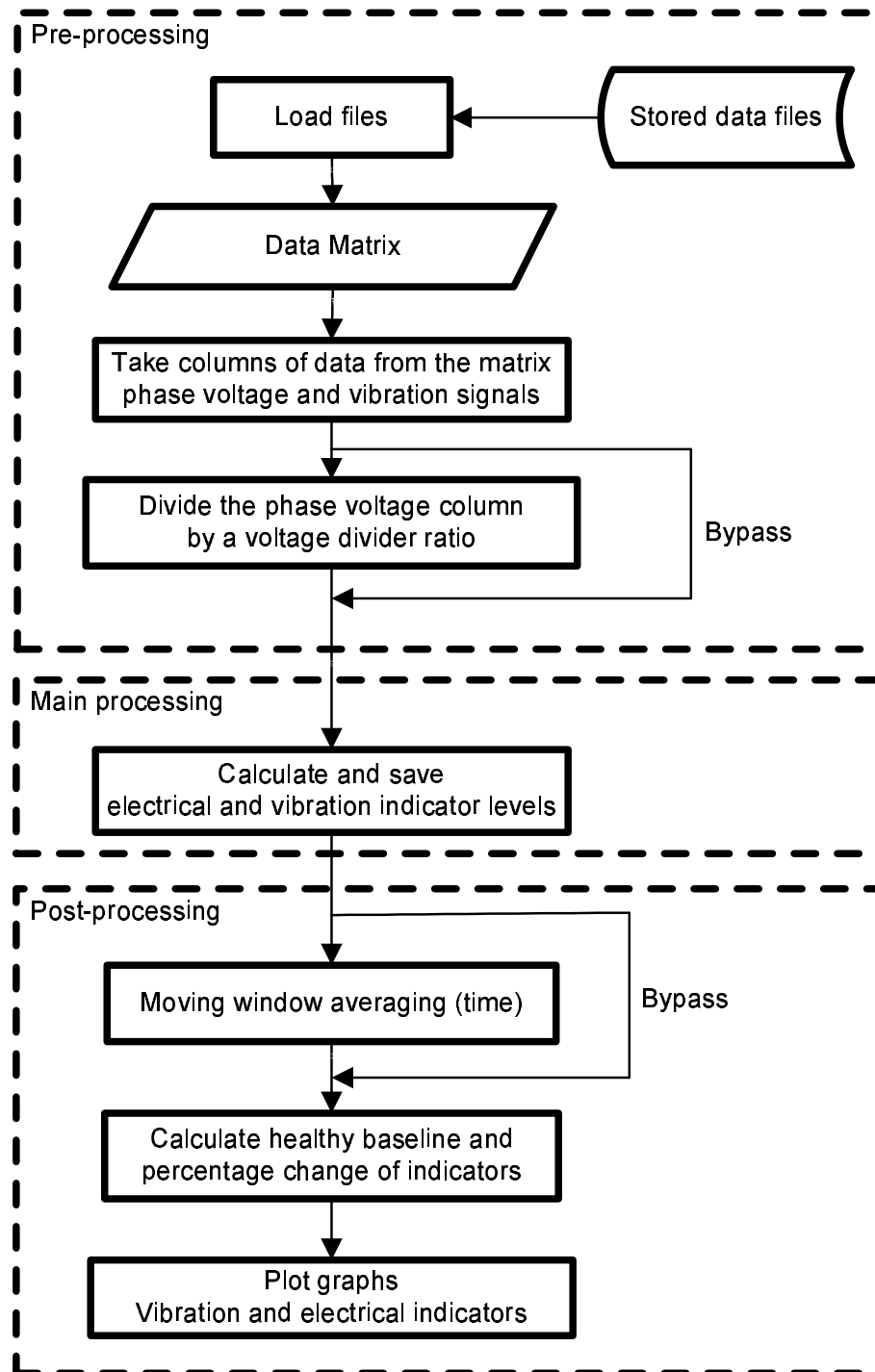


Fig. 11. Data processing flow chart.

Each routine is explained in the following sub-sections.

### 1. Pre-processing Routine

The objective of the pre-processing routine is to condition the raw armature phase voltage signals and the raw vibration signals. The NI DAQ program saves the experimental data into text files. The text file contains columns of the raw experimental data, and each of the columns corresponds to a single channel of signal samples for 30 seconds of sampling time. In this routine, each data file is loaded and saved into a raw data matrix. Then the columns that correspond to the two armature voltages and the three vibration signals are copied from the matrix and stored in separate columns. The voltage column vectors are divided by the step-down scale of the PT voltage divider so that they represent the real armature phase voltage values at the generator terminals. The vibration signals bypass this procedure.

### 2. Main Processing Routine

The objective of the main processing routine is to calculate an average health indicator and an average vibration indicator. This routine is divided into the time domain processing and the frequency domain processing. A detailed flow chart of the main routine is depicted in Fig. 12. The detailed procedures are explained below.

#### a. Time Domain Processing for Electrical Health Indicator Calculation

The health indicator calculation consists of several data processing steps in the time domain. First, the bias of the armature voltage signals is removed in the time domain. At this step, only the DC component of the signals is removed using a bias removal process. The bias removal process is performed using the following equation:



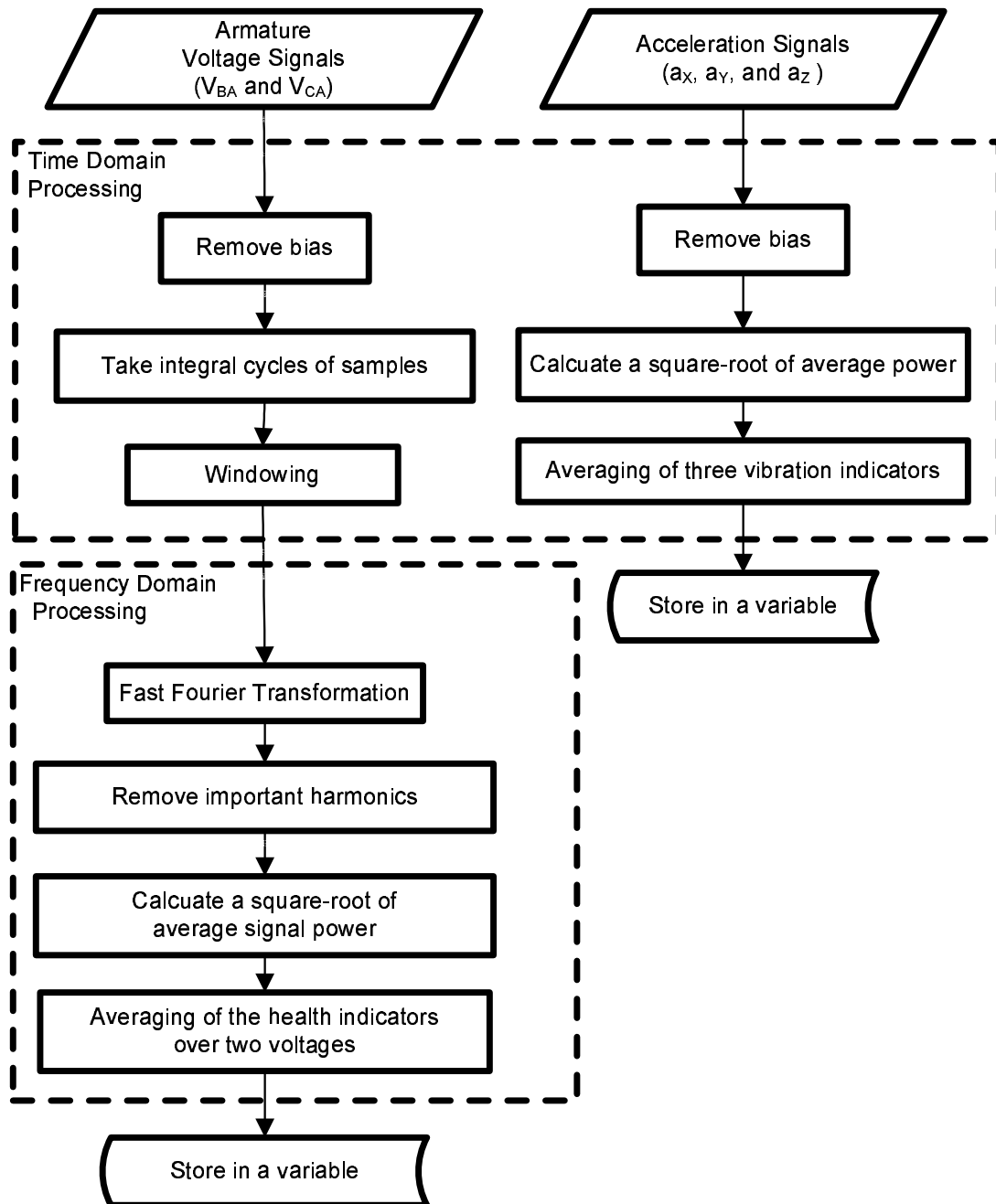


Fig. 12. Flow chart of the main data processing routine.

$$v_{i,I} = v_i - \frac{\sum_{j=1}^N v_j}{N} \quad (4.2)$$

where  $i=1\dots N$ ,  $v_i$  and  $v_{i,I}$  are the  $i$ -th voltage sample before and after a bias removal, and  $N$  is the total number of sampling points in the signal.

Before converting the time domain signals into the frequency domain, two steps are taken in order to minimize spectral leakage. In the first step, an integral number of cycles of the voltage samples are taken from the unbiased signals using the zero-crossing process. In the process, the samples before the first zero-crossing point are discarded. The slope sign in the first zero-crossing point is recorded. The last zero-crossing point in the data set that has the opposite slope sign than the first zero crossing is searched. The samples after the last zero-crossing point, including the zero crossing point itself, are discarded. Therefore, the total number of samples becomes  $M$ .

The FFT without the application of a proper window introduces ripples over pass and stop bands, and oscillatory behavior at band edges, best known as Gibbs phenomenon [39]. After testing several windows, such as the Hanning and Kaiser windows, it is found that the Blackman window gives the best performance in terms of side bands and a frequency resolution. Hence, the time signal is multiplied by a Blackman window of the size of  $M$ . This point by point multiplication step is described in the following equation:

$$v_{i,II} = v_{i,I} \times w_i \quad (4.3)$$

$$= v_{i,I} \times \left[ 0.42 - 0.5 \times \cos\left(\frac{2\pi i}{M-1}\right) + 0.08 \times \cos\left(\frac{4\pi i}{M-1}\right) \right] \quad (4.4)$$

where  $i=1\dots N$ ,  $v_{i,II}$  and  $v_{i,I}$  are the  $i$ -th voltage samples before and after windowing,

$w_i$  is the  $i$ -th Blackman window sample. Blackman window has a relatively wider transition band of  $\frac{12\pi}{M}$ , yet its smallest peak sidelobe, which is -58 dB [39]. Given that  $M$  is about  $2 \times 10^5$  in this research, the adversary effect of three time wider transition width of main lobes compared to the rectangular window can be negligible. A comparison graph of the voltage signature with and without the windowing process is depicted in Fig. 13.

#### b. Frequency Domain Processing for Electrical Health Indicator Calculation

After the leakage minimization process, the FFT of the conditioned voltage signals is performed. It is known that there are limitations in using the FFT for non-stationary signals, such as armature current and voltage signals. Though the wavelet transform (WT) may be one of the best signal processing tools for the analysis of non-stationary signals, in this research it is desired to eliminate or average the non-stationary parts of the signals involved; they do not carry any fault relevant information. The decision to use the FFT algorithm is based on the fact that the rms of the voltage signals do not vary more than  $\pm 5\%$  from the average rms value. In addition, it is observed that the amplitude and frequency of the large odd harmonics in the armature voltage signature remain within  $\pm 5\%$  of the average in an experiment.

The fundamental harmonic has the largest amplitude in the voltage signature. The fundamental frequency of the voltage is identified based on this characteristic. It is observed that the fundamental electrical frequency is slightly higher than six times of the inverter set-point frequency. This is because the rotor has six pole pairs and the pitch diameter of the driven sheave is slightly smaller than the driving sheave's pitch diameter.

The odd harmonics are notched out from the voltage signatures by simply removing an appropriate frequency band around each odd harmonic frequency. Removing

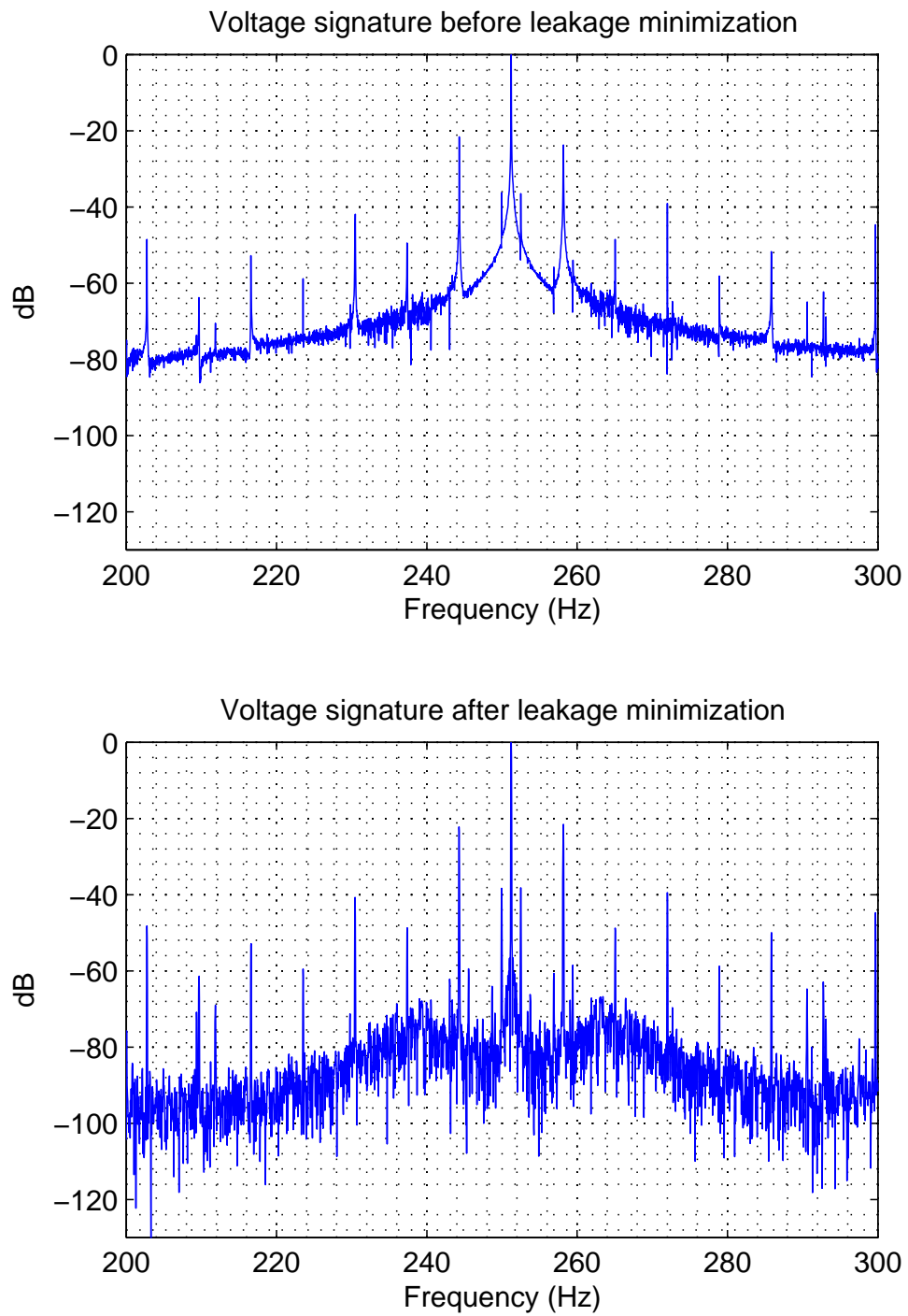


Fig. 13. Voltage signatures before and after leakage minimization at 40 Hz operation.

the large odd harmonics allows the changes in the rest of the voltage signatures to be more evident. The notching process is performed in the frequency domain rather in the time domain due to harmonic distortions and computational efficiency. If a time domain notching process is applied, a very high order notch filter is required due to a narrow notching band. After trial and error, it is observed that oscillatory behavior at band edges near the large odd harmonics is difficult to avoid when even using a very higher order notch filter. The selection of the notch filter order causes another complication when automating this process.

There exist discernible multiple sidebands found around the odd harmonics. The sidebands around the odd harmonics are removed in the same manner as the odd harmonics.

The origin of the multiple sidebands may be related to the soft coupling considering the fact that the sidebands are found at the frequencies where the belt harmonics are modulated by the large odd harmonics of the phase voltage. The modulation process is similar to that of single point bearing defect frequencies. The single point bearing defect frequency components are found at frequencies where a mechanical vibration frequency is modulated by the fundamental electrical supply frequency [9]. The belt fundamental frequency can be estimated as follows: The belt has 45 inch circumferential length and the pitch diameter of the sheaves is approximately 2.4". Therefore, the speed ratio between the belt and the sheave becomes about 6 assuming that there is no slip between them. When the inverter speed setting is, for example, at 40 Hz, then the driven sheave in the generator rotates approximately at 42 Hz. Considering the speed ratio, the rotational frequency of the V belt can be estimated to be about 7.0 Hz.

The remaining frequency signature is then used for the calculation of an electrical health indicator. A square root of an average power of the remaining signature is

calculated based on the following equation:

$$X_{E \text{ indicator}} = \frac{\sqrt{\sum_{j=L}^M |\mathbf{V}_j|^2}}{M - L + 1} \quad (4.5)$$

where  $\mathbf{V}_j$  is the j-th frequency signature component of the voltage signal, L is the index of signature component corresponding to 4 Hz, and M is the total number of frequency signature components. It is noted that the frequency signature components over 4 Hz are counted in the calculation. It is because there still exist some very low frequency components in the remaining signature due to the grounding connection in the PT and counting components above 4 Hz can ease the computational burden.

Each file has two channels of the armature voltages. Therefore, two electrical fault indicators are calculated and then they are averaged. The average electrical fault indicator is stored in a vector variable for later comparison.

### c. Vibration Indicator Calculation

The vibration indicator calculation starts with the aforementioned bias removing process. After the bias removal process, a square root of an average power of the conditioned vibration signal is calculated in time domain based on the following equation:

$$X_{vibration} = \sqrt{\frac{\sum_{j=1}^N |a_j|^2}{N}} \quad (4.6)$$

where  $a_j$  is the j-th acceleration sample and N is the total number of acceleration samples. Each file has three columns of the vibration signals. So three vibration indicators are calculated. The three vibration are averaged and stored in a variable vector.

### 3. Post-processing Routine

#### a. Moving Window Averaging

The purpose of the moving window averaging (MWA) process is to smooth the locus of the electrical fault indicator in an experimental period. It is found that the healthy variation on the electrical indicator exceeds a  $\pm 5\%$  margin in some experiments. One of the reasons for the over 5% healthy variation is that the remaining frequency signature after a series of harmonic removal processes still contains the frequency components unrelated to the bearing condition, which are typically non-stationary.

The overlap size of the moving window is set at 1 point for both 20 Hz and 40 Hz groups. The moving window size is set at 12 points for the 40 Hz group and 48 points for the 20 Hz group, both found by trial and error. The reason for a larger window for the 20 Hz group is that the healthy variations of the group are larger than the healthy variations of the 40 Hz group. On the contrary, the vibration indicator in the healthy period does not show variation of more than  $\pm 5\%$ . Hence, no MWA process is applied to the vibration indicator. From this point, the electrical indicator refers to a moving window averaged electrical indicator.

#### b. Comparison Method

Since there exist variations on the healthy indicator regardless of applying the MWA process, the mean value of 48 indicator values in the healthy period is chosen to represent the healthy baseline value. The baseline is calculated as follows:

$$X_{baseline} = \frac{\sum_{j=1}^{48} X_j}{48} \quad (4.7)$$

where  $X_j$  is the  $j$ -th electrical or vibration indicator. The electrical and vibration baselines of the experiments are summarized in Table III. The unit of the vibration

indicator is G, the gravitational acceleration, which is converted using the conversion ratio of 100 mV per G from the accelerometer specifications.

Table III. Comparison of healthy baselines.

Group	20 Hz		40 Hz	
Experiment Number	Electrical (mV)	Vibration (G)	Electrical (mV)	Vibration (G)
1	60.4	n/a	62.9	n/a
2	61.2	n/a	62.7	n/a
3	61.9	0.23	64.4	n/a
4	60.4	0.30	73.2	0.59
5	58.6	0.23	66.6	0.51
Mean	60.5	0.25	66.0	0.55
Standard Deviation (S.D.)	1.2	0.04	4.3	0.06
S.D. / Mean	2.0%	16%	6.5%	11%

Table III shows that there exist considerable variations on the healthy baselines even in the same group. One of the reasons for the variations is that the inevitable reassembly and reinstallation processes of the generator between experiments cause considerable changes in the armature voltage signatures and the machine vibration level as discussed in [31]. Therefore, setting a common universal electrical or vibration baseline level is impractical.

Due to the varying baselines, a different electrical or vibration healthy baseline is set for each of the experiments. In order to compare the results of different experiments, the indicator percent changes in an experiment are calculated as follows: First, the healthy baseline of an experiment is calculate by averaging all the 48 pre-MWA



indicator values in a healthy period. The indicator percentage change compared to the healthy baseline is computed as follow:

$$\widetilde{X}_k = \frac{\widehat{X}_k - X_{baseline}}{X_{baseline}} \times 100 \quad (4.8)$$

where  $\widetilde{X}_k$  is the percentage change of the k-th indicator,  $\widehat{X}_k$  is the k-th electrical indicator or the k-th vibration indicator, and  $X_{baseline}$  is the healthy baseline of the experiment.

### c. Bearing Fault Detection Effectiveness

The objective of this research is in demonstrating the effectiveness of the proposed analysis method in detecting bearing problems. A signature variation of more than 5% is declared to represent a faulty bearing. This detection guideline is consistently applied to the electrical and vibration indicators of all the experiments.

## C. Analysis of Experimental Results

The detailed data processing routines are explained in the previous section. This section focuses on the result analysis. First, the bearing fault detection capability of the electrical indicator is demonstrated. Then, the bearing fault detection time of the electrical indicator is analyzed and its performance is compared to that of the vibration indicator.

### 1. Demonstration of Bearing Fault Detection

The comparison plots in this section show the electrical indicator percentage change (E IPC) and the vibration indicator percentage change (VIB IPC) on the same plot in order to demonstrate the bearing fault detection capability of the electrical indicator.

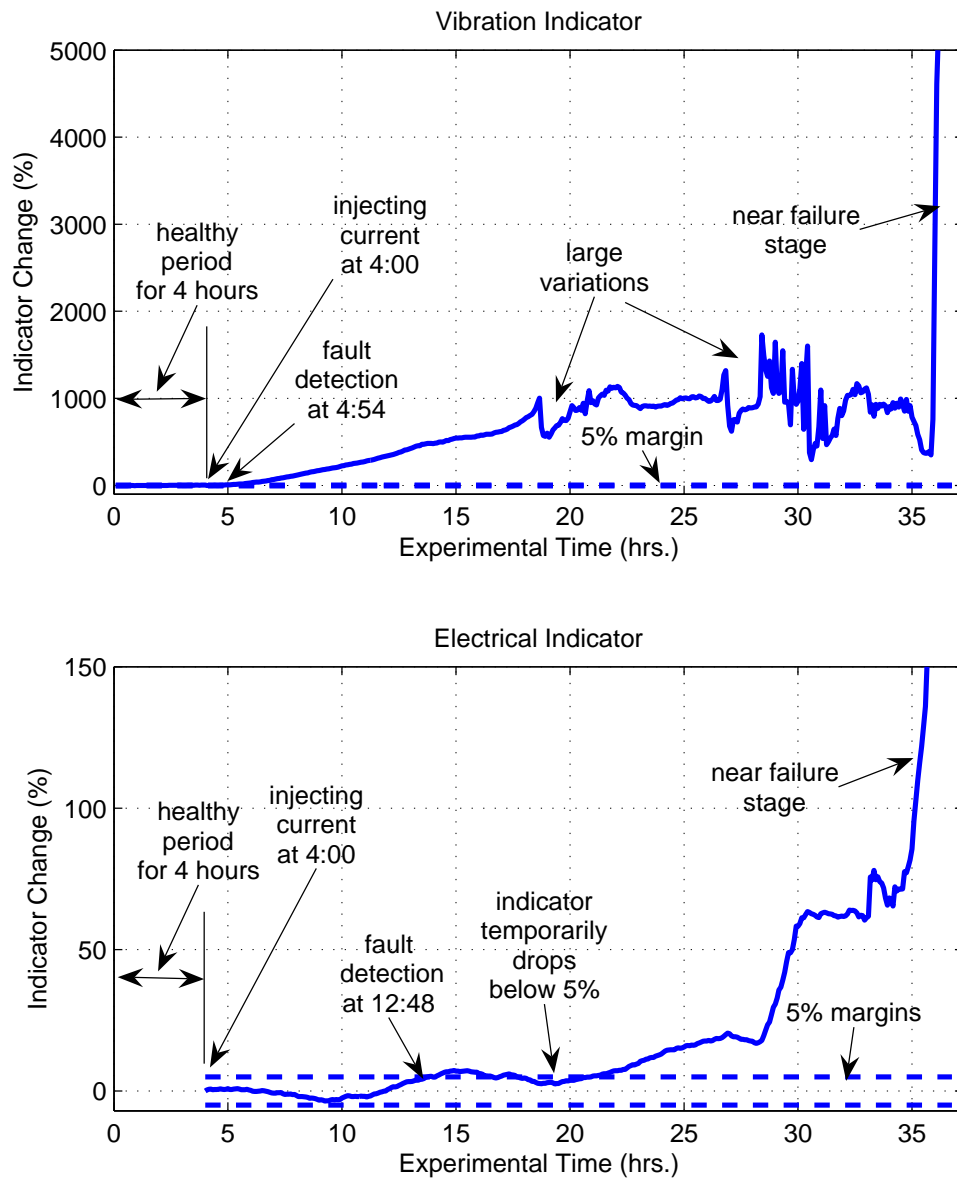


Fig. 14. Indicator comparison plot for a 20 Hz case study; experiment #3.

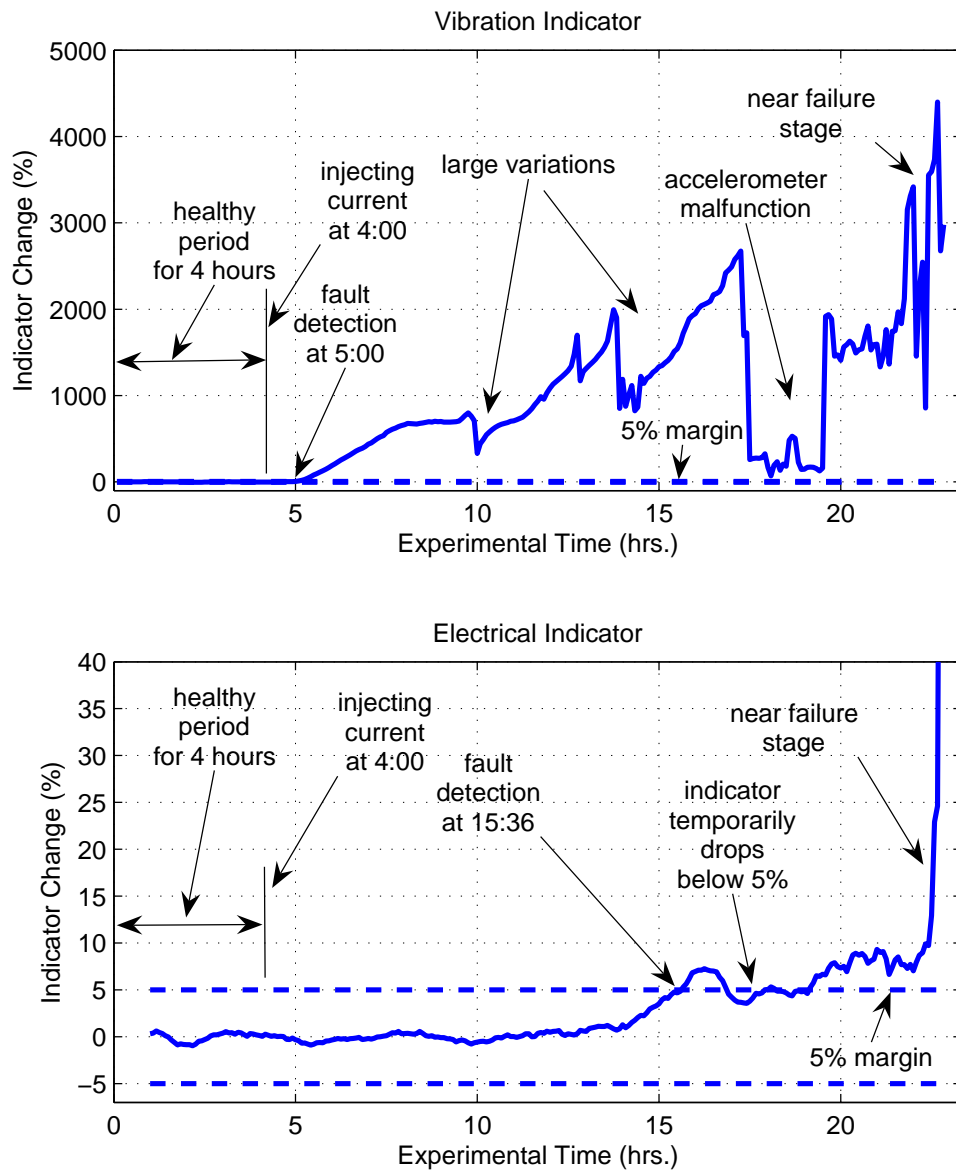


Fig. 15. Indicator comparison plot for a 40 Hz case study; experiment #4.

A comparison plot for a 20 Hz case study is depicted in Fig. 14. The VIB IPC remains within a  $\pm 5\%$  range for the 4 hour healthy period. The VIB IPC starts to increase after injecting the bearing damage current. This trend continues till the middle of the experiment. Then the large variations on the VIB IPC start to appear while the VIB IPC remains approximately at 1000%. The VIB IPC shows oscillatory behavior before the near failure stage. Then it skyrockets to thousands of percent. Usually at this stage, the synchronous generator runs roughly and the bearing causes excessive noise. Then the experiment is halted.

A similar trend is found in the E IPC graph. It is noted that the first four hours of the E IPC is missing in the graph since the first E IPC value can be computed after collecting the first 48 data files. Hence, there exists only one pure healthy E IPC value. So the healthy variations are not comparable. The E IPC remains within a  $\pm 5\%$  range for the next several hours after the healthy period. This may be because most of the pre-MWA electrical indicator values in the healthy period remain within the  $\pm 5\%$  margin and there is no sudden increase of this indicator until a few hour after the initiation of the *in-situ* bearing damage process. Then, the E IPC starts to increase steadily while showing some variations. The steadily growing trend continues until the first jump of the E IPC appears a few hour before the near failure. Then the E IPC reaches about 65% and then it skyrockets up to hundreds of percents.

A comparison plot for a 40 Hz case study is depicted in Fig. 15. This comparison plot shows the generally similar trend compared to the 20 Hz case study discussed above. The healthy E IPC remains within the  $\pm 5$  margin. One noticeable difference compared to the previous comparison plot is that the E IPC barely reaches 10% margin before the near failure stage. However, it is observed that this trend is not consistent in the 40 Hz group. As seen in Fig. 16, the E IPC exceed 20% even before the near failure stage and never drops below 20%.

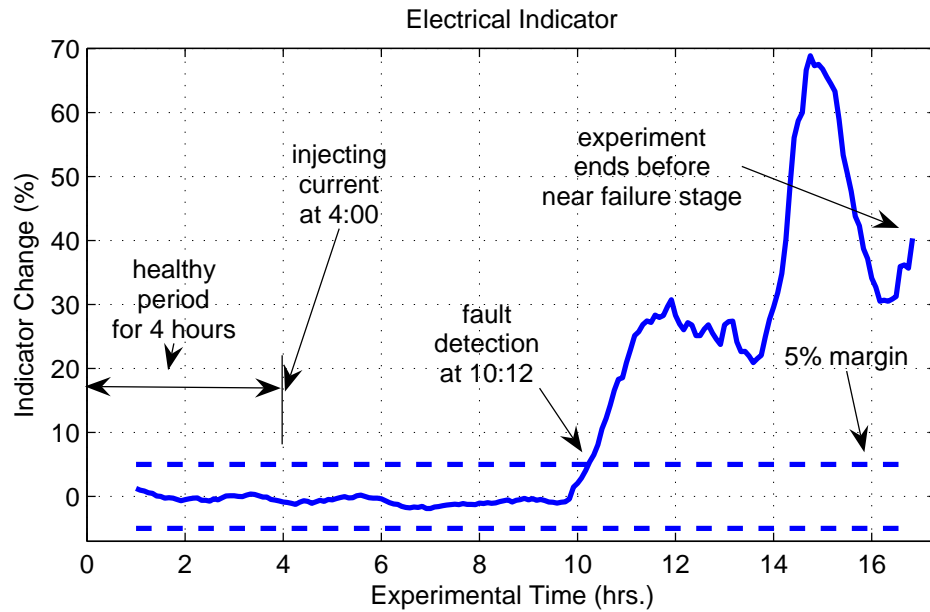


Fig. 16. Electrical indicator plot for a 40 Hz case study; experiment #1.

There are some experiments that are halted before the near failure stage due to time constraints. One example is depicted in Fig. 17. One noticeable difference from the above mentioned comparison plots is that the VIB IPC does not skyrocket near the end of experiment though it is still 1500% higher than the healthy baseline.

Fig. 18 shows the locus of the E IPC of another 20 Hz case study. The overall increase trend of the E IPC before the near failure stage resembles to that of Fig. 17. The E IPC remains within the  $\pm 5$  margin for several hours after the initiation of the bearing damage process. The E IPC starts to climb at about 17:00. The increase rate of the E IPC slows down in a few hours after the E IPC passes the 5% margin. Then the E IPC decreases temporarily by about 10%. It is noted that the E IPC never drops below the 5% margin after the fault detection.

It is observed that not all the experiment results show the above mentioned

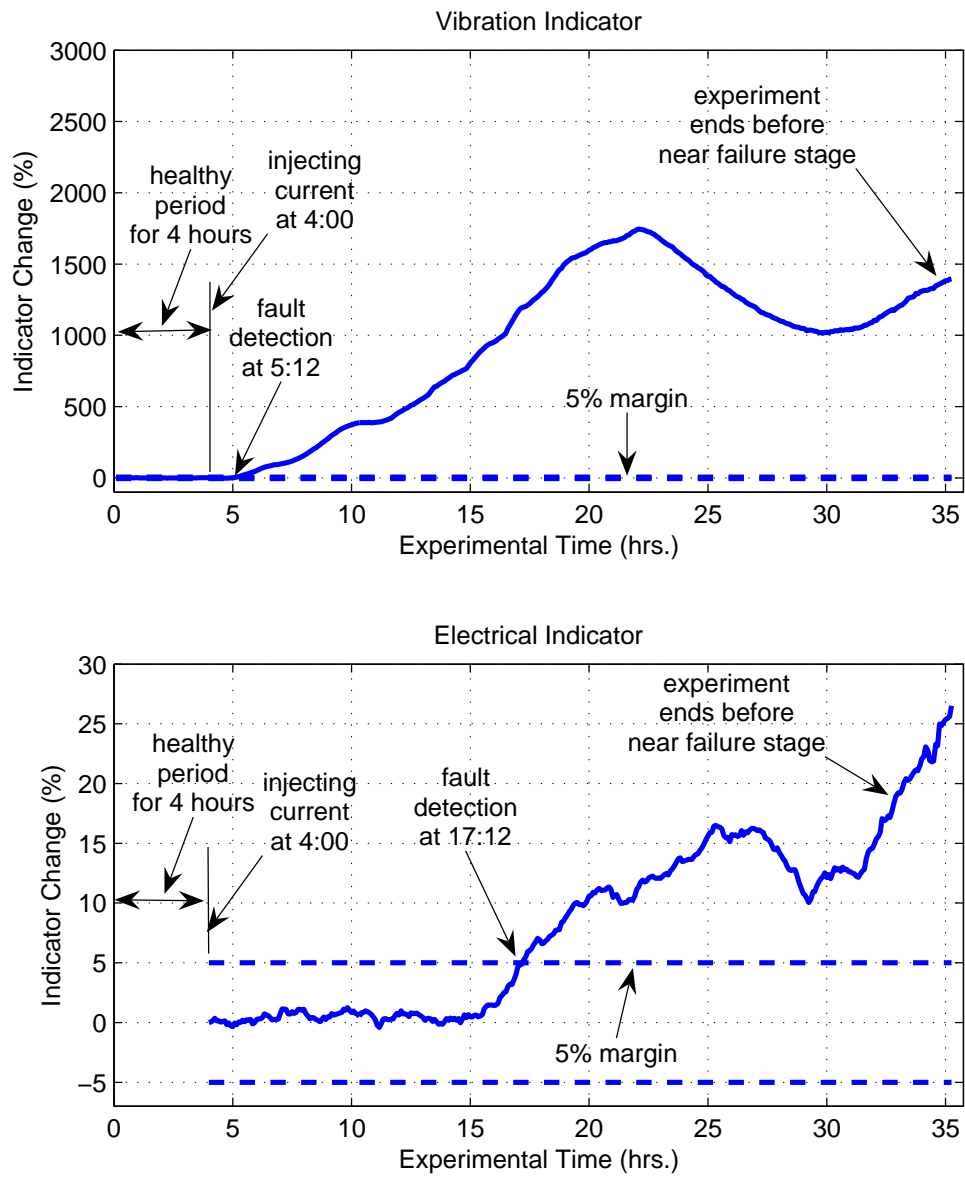


Fig. 17. Indicator comparison plot for a 20 Hz case study; experiment #4.

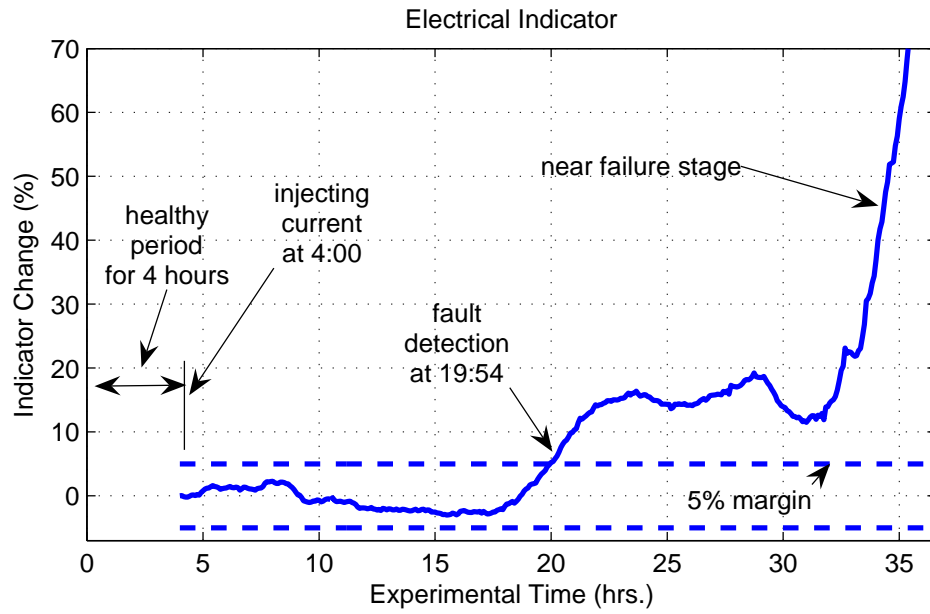


Fig. 18. Electrical indicator plot for a 20 Hz case study; experiment #2.

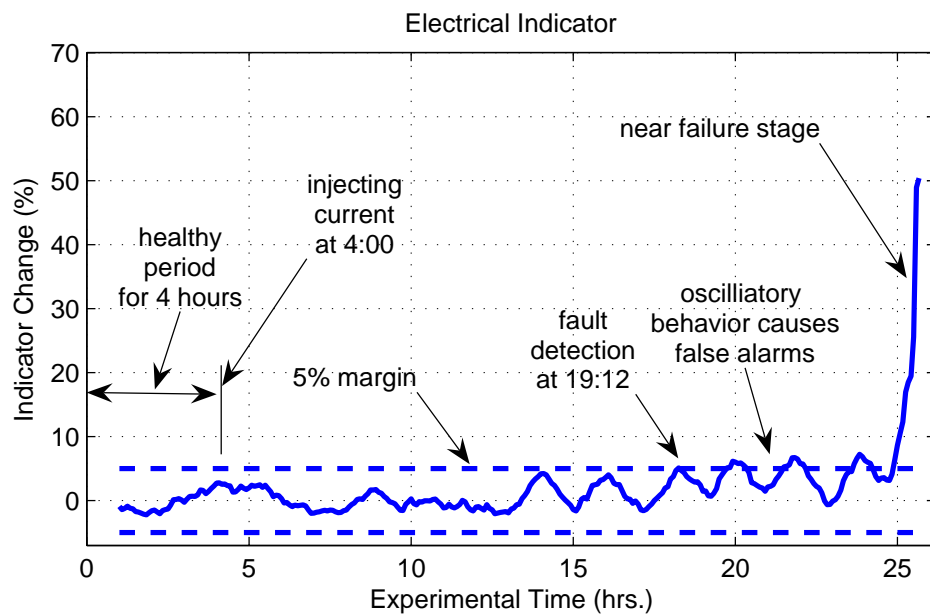


Fig. 19. Electrical indicator plot for a 40 Hz case study; experiment #5.

types of bearing deteriorating trends. The E IPC in Fig. 19 shows highly oscillatory behavior a few hours after the *in-situ* bearing damage process starts. This trend could cause false alarms and delay bearing fault detection. The E IPC increases in an oscillatory manner and exceeds the 5% margin. Finally, it skyrockets at the near failure stage.

## 2. Time Acceleration Scale

Since an accelerating bearing damage process is utilized in this research, it can be meaningful to roughly estimate the time acceleration scale. The average bearing failure times in the experiments performed are first evaluated. Then the average bearing failure detection time in practice is estimated.

The generator runs roughly at the near failure stage. This sign is the basis of the experimental termination decision. The bearing failure time are summarized in Table IV. The bearing failure time refers to the time spent in fully damaging the front bearing. Therefore, the pre-running time and healthy period are not included in the calculation. It is noted that some experiments are not counted since they are halted before a near failure stage. In those experiments, neither a sign of the immanent bearing failure nor a dramatic increase in the vibration level are observed.

The bearing failure mode under the influence of shaft current is different from the normal bearing failure mode. Therefore, the  $L_{10}$  bearing life formula is not used in this study. According to field experience, a typical bearing failure time for this type of failure mode is about 6 to 12 months, with an expected failure period of 9 months.

Assuming the typical real world bearing failure time from on-set of a fault to be 9 months, the time acceleration scale becomes 212 for the 20 Hz group and 343 for the 40 Hz group. Therefore, the moving window size in the real world time scale is



Table IV. Comparison of bearing failure times.

Exp#	Bearing Failure Time (hrs.)	
	20 Hz Group	40 Hz Group
1	26.8	n/a
2	32.1	17.7
3	32.8	17.5
4	n/a	18.8
5	n/a	21.7
Mean	30.6	18.9
Standard Deviation (S.D.)	3.2	1.9
S.D. / Mean	10%	10%

35.3 days for the 20 Hz group and 14.3 days for the 40 Hz group. The overlapping size in the real world time scale is 0.7 day for the 20 Hz group and 1.2 day for the 40 Hz group.

### 3. Performance Analysis

The estimated bearing fault detection times using the electrical indicator and the vibration indicator are summarized in Table V. It is noted that vibration data are not collected in the first five experiments, therefore, no bearing fault detection can be inferred.

The average bearing fault detection time of the electrical indicator method is roughly 10 times that of the vibration indicator method in this research. As seen in the comparison table, the average increase rate of the VIB IPC after the initiation of the *in-situ* bearing damage process is far larger than that of the E IPC. Moreover,

Table V. Comparison of estimated bearing fault detection times.

Exp#	Bearing Fault Detection Time (hrs.)			
	20 Hz Group		40 Hz Group	
	Electrical	Vibration	Electrical	Vibration
1	20.7	n/a	6.2	n/a
2	15.9	n/a	11.6	n/a
3	8.8	0.9	6.9	n/a
4	13.2	1.2	11.6	1.0
5	2.0	0.6	14.2	0.4
Mean	12.1	0.9	10.1	0.7
Standard Deviation (S.D.)	7.1	0.3	3.4	0.4
S.D. / Mean	59%	33%	34%	57%

there exists only a small variation on the VIB IPC. These two factors contribute to early bearing fault detection with the vibration method. However, the E IPC shows a sluggishly increasing trend and a relatively larger variation. In addition, the electrical indicator method requires the moving window averaging process. All these factors contribute to the slow detection time using the electrical indicator.

The similar average fault detection time of the two case studies shows that in the bearing failure mode studied in this research, the bearing speed is not a major factor in deciding the time when the bearing fault starts to appear on the raceways. According to [32], the time when flutes appear on the raceways under the influence of a shaft current is determined by the bearing dimensions, the material strength properties, the initial roughness on the raceways, and the current magnitude. The consistent bearing damage current setting throughout the experiments may have resulted in the

similar average fault detection time for both case studies, 20 Hz and 40 Hz.

The high electrical indicator variation may result from the presence of non-stationary frequency components unrelated to the bearing condition in the remaining voltage signatures. It is noted that the bearing fault indicator proposed in [25] has the improved robustness against the major disturbances by notching out the major frequencies unrelated to the bearing health during the calculation process. However, the notching processes presented in that article requires full knowledge of machine & bearing parameters, information that may not be accessible in practice.

As seen from the previous plots, the large electrical indicator variation could cause the frequent false alarms. However, no false alarming prevention methods are studied in this research, as the objective of this research lies more in the demonstration of bearing fault detection capability of the electrical indicator.

The bearing fault detection capability of the electrical indicator can be demonstrated statistically. The average bearing failure times for the 20 Hz group and the 40 Hz group are 30.6 hours and 18.9 hours, respectively. The average fault detection times are 12.1 hours for the 20 Hz group and the 10.1 hours for the 40 Hz group. Considering the detection time variability within two standard deviations, the fault detection times become 26.3 hours for the 20 Hz group and 16.9 hours for the 40 Hz group. Therefore, in most instances, the electrical indicator can detect the bearing fault before the bearing condition reaches near failure stage. These results show the feasibility of using this simple electrical indicator for detection of bearing faults in synchronous generators. The results presented are statistically significant.

#### D. Chapter Summary

In this chapter, the data processing routines are explained in detail. The result plots demonstrate the bearing detection capability of the proposed electrical method as compared to a vibration indicator. The bearing fault detection capability in different operating conditions is also examined. The bearing fault detection times are analyzed statistically.

## CHAPTER V

### SUMMARY AND CONCLUSIONS

This chapter summarizes the discussions presented in the previous chapters. The conclusions from this research are summarized. Finally recommendations for future research work in this area are outlined.

#### A. Summary of Research

The main objective of this research is to demonstrate the bearing fault detection capability of the proposed electrical indicator. A generator test bed with *in-situ* bearing damage device is designed and built. Ten experiments with different operating conditions are conducted while the bearing failure is accelerated using the *in-situ* bearing damage circuit. The electrical indicator is computed using the armature voltage signals without the aid of machine parameters. The vibration indicator is calculated based on the acceleration data. The bearing fault detection capability of the electrical indicator is demonstrated in different operating conditions, and compared to the vibration indicator. The performance of the electrical indicator is analyzed with respect to the fault detection time.

In Chapter I, the necessity of a sensorless, electrical bearing fault detection method in synchronous generators is discussed. The literature review, the proposed method, and the research objectives are summarized.

Chapter II presents an overview of the experimental setup used in this research. The design points, the operating principles, and the specifications of the experimental equipment are described. This chapter also focuses on the installation and assembly details to minimize the effects of mechanical disturbances unrelated to bearing faults.

Chapter III discusses the experimental procedures. The detailed preparatory

procedures are described first. Then, the experimental plan is presented and the equipment parameter settings are summarized.

In Chapter IV, the detailed data processing routines are described. Then the experimental data are analyzed. The bearing fault detection capability of the electrical indicator is demonstrated in comparison to the vibration indicator. The performance of the proposed electrical fault detection method is analyzed.

## B. Conclusions

The research conclusions are summarized as follows:

- Rolling element bearing faults in synchronous generators can be detected using the proposed method based on electrical signatures.
- The proposed approach is independent of machine and bearing specific parameters.
- The bearing fault detection method is independent of the machine operating conditions.

## C. Recommended for Future Research Work

The performance of the electrical indicator shows the necessity for further research to improve the detection time and possible false alarms. Some possible future research topics are:

1. To study the effects of the bearing damage current on the stator output measurements; the large bearing damage current itself could be causing significant harmonic distortion to generator voltage signatures.

2. To reduce the variability of the electrical indicator without using machine and/or bearing parameters.
3. To establish bearing fault detection criteria based on blind detection.

## REFERENCES

- [1] I. Tabatabaei, J. Faiz, H. Lesani, and M. T. Nabavi-Razavi, "Modeling and simulation of a salient-pole synchronous generator with dynamic eccentricity using modified winding function theory," *IEEE Transactions on Magnetics*, vol. 40, no. 3, pp. 1550-1555, May 2004.
- [2] J. Penman and H. Jiang, "The detection of stator and rotor winding short circuits in synchronous generators by analyzing excitation current harmonics," *IEE Conference Publication*, no. 419, pp. 137-142, 1996.
- [3] C. A. Smith, M. D. Donovan, and M. J. Bartos, "Reliability survey of 600- to 1800-kW diesel and gas-turbine generating units," *IEEE Transactions on Industry Applications*, vol. 26, no. 4, pp. 741-755, July/Aug. 1990.
- [4] P. Y. Du, J. Burnett, and S. M. Chan, "Reliability of standby generators in Hong Kong buildings," *IEEE Transactions on Industry Applications*, vol. 39, no. 6, pp. 1592-1595, Nov./Dec. 2003.
- [5] F.A. Wyczalek, "Market mature 1998 hybrid electric vehicles," *Aerospace and Electronic Systems Magazine, IEEE*, vol. 14, no. 3, pp. 41-44, March 1999.
- [6] A. Kawahashi, "A new-generation hybrid electric vehicle and its supporting power semiconductor devices," *in Proc. ISPSD '04*, 24-27 May, 2004, pp. 23-29.
- [7] U. Grasselli, "Reliability survey of standby generator by evaluation of maintenance service data," *in Proc. IEEE Industry and Commercial Power Systems Tech Conf.*, May 1-5, 1994, pp. 231-233.



- [8] P. F. Albrecht, J. C. Appiarius, R. M. McCoy, E. L. Owen, and D. K. Sharma, "Assessment of the reliability of motors in utility applications-updated," *IEEE Transactions on Energy Conversion*, vol. EC-1, no. 1, pp. 39-46, Mar. 1986.
- [9] R. R. Schoen, T. G. Habetler, F. Kamran, and R. G. Bartheld, "Motor bearing damage detection using stator current monitoring," *IEEE Transactions on Industry Applications*, vol. 31, no. 6, pp. 1274-1279, Nov./Dec. 1995.
- [10] S. Norose, "Monitoring of journal bearing failure through ferrographic oil analysis," *Journal of Japan Society of Lubrication Engineers*, vol. 33, no. 7, pp. 533-539, 1988.
- [11] A. Dadouche, M. S. Safizadeh, J. Bird, W. Dmochowski, and D. S. Forsyth, "A comparative study of air-coupled ultrasound sensor and accelerometer in detecting bearing defects," in *Proc. World Tribology Congress III -2005*, Washington DC, 12-16 Sep., 2005, pp. 893-894.
- [12] J. R. Nicholas, "Available electrical technologies for monitoring," *Iron and Steel Engineer*, vol. 75, no. 10, pp. 34-40, Oct. 1998.
- [13] V. V. Matveev, A. V. Nekrutkin, V. V. Okhrimenko, and G. B. Chernikov, "A system of thermal monitoring for the bearing of a hydrogenerator," *Elektricheskie Stantsii*, no. 9, pp. 75-77, Sep. 1978.
- [14] O. V. Thorsen, M. Dalva, "Methods of condition monitoring and fault diagnosis for induction motors," *European Transactions on Electrical Power*, vol. 8, no. 5, pp. 383-395, Sep./Oct. 1998.
- [15] H. A. Toliyat and N. A. Al-Nuaim, "Simulation and detection of dynamic air-gap eccentricity in salient-pole synchronous machines," *IEEE Transactions on*

- Industrial Applications*, vol. 35, no. 1, pp. 86-93, Jan./Feb. 1999.
- [16] B. Li, M. Chow, Y. Tipsuwan, and J. C. Hung, "Neural-network-based motor rolling bearing fault diagnosis," *IEEE Transactions on Industry Electronics*, vol. 47, no. 5, pp. 1060-1069, Oct. 2000.
- [17] S. Nandi and H. A. Toliyat, "Condition monitoring and fault diagnosis of electrical machines-a review," *in Proc. IEEE-IAS 1999 Annu. Meeting*, Phoenix, AZ, Oct. 3-7, 1999, vol. 1, pp. 197-204.
- [18] F. K. Choy, J. Zhou, M. J. Braun, and L. Wang, "Vibration monitoring and damage quantification of faulty ball bearings," *Journal of Tribology*, vol. 127, pp. 776-783, Oct. 2005.
- [19] C. W. Ayers, "Electrical signature analysis applications for non-intrusive automotive alternator diagnostics," *MFPT Technology Showcase Proceedings*, Mobile, AL, 1996, pp. 85-94.
- [20] R. C. Kryter and H. D. Haynes, "How to monitor motor-driven machinery by analyzing motor current," *Power Engineering*, vol. 93, no. 10, pp. 35-39, Oct. 1989.
- [21] R. C. Kryter and H. D. Haynes, "Condition monitoring of machinery using motor current signature analysis," *Sound and Vibration*, vol. 23, no. 9, pp. 14-21, Sep. 1989.
- [22] A. Bellini, F. Filippetti, G. Franceschini, C. Tassoni, G. B. Kliman, "Quantitative evaluation of induction motor broken bars by means of electrical signature analysis," *IEEE Transactions on Industry Applications*, vol. 37, no. 5, pp. 1248-55, Sept.-Oct. 2001.

- [23] M. Blödt, P. Granjon, B. Raiso, and G. Rostaing, "Models for bearing damage detection in induction motors using stator current monitoring," *IEEE International Symposium*, vol. 1, pp. 383-388, May 2004.
- [24] B. Yazici and G. B. Kilman, "An adaptive statistical time-frequency method for detection of broken bars and bearing faults in motors using stator current," *IEEE Transactions on Industry Applications*, vol. 35, pp. 442-452, Mar./Apr. 1999.
- [25] J. R. Stack, T. G. Habetler, and R. G. Harley, "Bearing fault detection via autoregressive stator current modeling," *IEEE Transactions on Industry Applications*, vol. 40, no. 3, pp. 740-747, May/June 2004.
- [26] L. Eren and M. J. Devaney, "Bearing damage detection via wavelet packet decomposition of the stator current," *IEEE Transactions on Instrumentation and Measurement*, vol. 53, no. 2, pp. 431-436, Apr. 2004.
- [27] İ. Y. Önel, K. B. Dalci, and İ. Senor, "Detection of outer raceway bearing defects in small induction motors using stator current analysis," *Sādhanā*, vol. 30, pp. 713-722, Dec. 2005.
- [28] L. M. Dickens, H. D. Haynes, and C. W. Ayers, "Method and apparatus for monitoring aircraft components," U.S. Patent 5,483,833, 16 Jan., 1996.
- [29] J. R. Stack, T. G. Habetler, and R. G. Harley, "Fault classification and fault signature production for rolling element bearings in electric machines," *IEEE Transactions on Industry Applications*, vol. 40, no. 3, pp. 735-739, May/June 2004.
- [30] A. M. Knight and S. P. Bertani, "Mechanical fault detection in a medium-sized

- induction motor using stator current monitoring,” *IEEE Transactions on Energy Conversion*, vol. 20, no. 4, pp. 753-760, Dec. 2005.
- [31] J. R. Stack, T. G. Habetler, and R. G. Harley, “Experimentally generating faults in rolling element bearings via shaft current,” *IEEE Transactions on Industry Applications*, vol. 41, no. 1, pp. 25-29, Jan./Feb. 2005.
- [32] H. Prashad, “Diagnosis of rolling-element bearings failure by localized electrical current between track surfaces of races and rolling-elements,” *Journal of Tribology*, vol. 124, no. 3, pp. 468- 473, July 2002.
- [33] D. F. Busse, J. M. Erdman, R. J. Kerkman, D. W. Schlegel, and G. L. Skibinski, “The effects of PWM voltage source inverters on the mechanical performance of rolling bearings,” *IEEE Transactions on Industry Applications*, vol. 33, no. 2, pp. 567-576, March/April 1997.
- [34] J. M. Erdman, R. J. Kerkman, D. W. Schlegel, and G. L. Skibinski, “Effect of PWM inverters on AC bearing currents and shaft voltages,” *IEEE Transactions on Industry Applications*, vol. 32, no. 2, pp. 250-259, March/April 1996.
- [35] R. Ramshaw and R. G. van Heeswijk, *Energy Conversion: Electric Motors and Generators*. Orlando, FL: Saunders College Publishing, 1990.
- [36] K. G. Büger, *Alternators.*, Stuttgart, Germany: Robert Bosch GmbH, 1999.
- [37] H. Prashad, “Diagnosis of failure of rolling-element bearings of alternators-a study,” *Wear*, vol. 198, no. 1-2, pp. 46-51, Oct. 1996.
- [38] H. Prashad, “Investigation of damaged rolling element bearings and deterioration of lubricant under the influence of electric field,” *Wear*, vol. 176, no. 2, pp. 151-161, Aug. 1994.

- [39] J. G. Proakis and D. G. Manolakis, *Digital Signal Processing.*, Delhi, India: Pearson Education, 2004.

## VITA

The author, Jae-Won Choi, was born in Busan, South Korea. He received his Bachelor of Engineering degree in Mechanical Engineering from Korea University, Seoul, Korea in February 2003. From Fall 2003 onwards he pursued the Master of Science degree program in the Mechanical Engineering Department, Texas A&M University, College Station and received his degree in December 2006.

Permanent Address:

Jae-Won Choi

9/2, 17-5 byunji, Youngju 1 dong, Jung ku,

Busan, South Korea, 600-811

Phone: (082) 051-4696730

Email: [jwchoi@tamu.edu](mailto:jwchoi@tamu.edu)